

Projection depth for functional data: Practical issues, computation and applications

Filip Bočinec^a, Stanislav Nagy^a, Hyemin Yeon^b

^a*Faculty of Mathematics and Physics, Charles University, Prague, Czech Republic*

^b*Department of Mathematical Sciences, Kent State University, Kent, USA*

Abstract

Statistical analysis of functional data is challenging due to their complex patterns, for which functional depth provides an effective means of reflecting their ordering structure. In this work, we investigate practical aspects of the recently proposed regularized projection depth (RPD), which induces a meaningful ordering of functional data while appropriately accommodating their complex shape features. Specifically, we examine the impact and choice of its tuning parameter, which regulates the degree of effective dimension reduction applied to the data, and propose a random projection-based approach for its efficient computation, supported by theoretical justification. Through comprehensive numerical studies, we explore a wide range of statistical applications of the RPD and demonstrate its particular usefulness in uncovering shape features in functional data analysis. This ability allows the RPD to outperform competing depth-based methods, especially in tasks such as functional outlier detection, classification, and two-sample hypothesis testing.

Keywords: functional data analysis, statistical depth, projection depth, robust statistics

2020 MSC: 62G05, 62H99, 62R10

1. Introduction: Regularized projection depth

Over the past two decades, the ordering structure of functional data has been extensively studied, leading to many effective applications in Statistics and Machine Learning. A central concept is functional depth, an extension of multivariate depth functions such as halfspace (Tukey, 1975), simplicial (Liu, 1990), spatial (Chaudhuri, 1996), and zonoid (Mosler, 2002) depths, which measures centrality versus outlyingness for functional data. Examples of functional depths include integrated (Fraiman and Muniz, 2001), (modified) band (López-Pintado and Romo, 2009), infimal (Mosler, 2013), spatial (Chakraborty and Chaudhuri, 2014b) and spherical (Elmore et al., 2006; Mendroš and Nagy, 2025) depths. All these depths naturally induce rankings and support a variety of statistical tools for functional data analysis (Hubert et al., 2017; Sun and Genton, 2011; Ramsay and Chenouri, 2024;

Email addresses: bocinec@karlin.mff.cuni.cz (Filip Bočinec), nagy@karlin.mff.cuni.cz (Stanislav Nagy), hyeon1@kent.edu (Hyemin Yeon)

Chakraborty and Chaudhuri, 2014a). An important distinction from multivariate data is that functional data may often exhibit complex *shape* patterns. This makes analysis more difficult and hence motivates the development of depth measures that are more sensitive to shape-related features (Hlubinka et al., 2015; Nagy et al., 2017; Helander et al., 2020; Yeon et al., 2025).

Recently, Boćinec et al. (2026) (hereafter **[B]**) extended the prominent projection depth on the Euclidean space (Zuo, 2003) to an infinite-dimensional separable Hilbert space \mathbb{H} . The projection depth builds on the paradigm of projection pursuit (Huber, 1985) and the Stahel-Donoho outlyingness (Stahel, 1981; Donoho, 1982). To explain, let $\langle \cdot, \cdot \rangle$ be the inner product for \mathbb{H} with induced norm $\|\cdot\|$, and we denote by $\mathcal{P}(\mathbb{H})$ the set of Borel probability measures on \mathbb{H} . For $x \in \mathbb{H}$ and a unit vector $v \in \mathbb{S} = \{y \in \mathbb{H} : \|y\| = 1\}$, the outlyingness of x with respect to $X \sim P_X \in \mathcal{P}(\mathbb{H})$ in direction v is

$$O_v(x; P_X) = \frac{|\langle x, v \rangle - \text{med}[\langle X, v \rangle]|}{\text{MAD}[\langle X, v \rangle]}, \quad (1)$$

where $\text{med}[U]$ and $\text{MAD}[U]$ denote the median and median absolute deviation of a real-valued variable U .¹ **[B]** notice that the maximal outlyingness (over all directions $v \in \mathbb{S}$) can be infinite almost everywhere. This yields a degenerate projection depth in \mathbb{H} , which is not statistically useful for functional data analysis. To address this degeneracy, **[B]** develop the *regularized projection depth* (**RPD**) by incorporating a regularization that ensures well-defined and strictly positive values, as defined below.

Definition (Regularized projection depth, **[B]**). For $\beta \geq 0$ and $X \sim P_X \in \mathcal{P}(\mathbb{H})$, we consider the regularized set of directions

$$\mathcal{V}_\beta = \mathcal{V}_\beta(P_X) = \{v \in \mathbb{S} : \text{MAD}[\langle X, v \rangle] \geq \beta\}. \quad (2)$$

The *regularized projection depth* (**RPD**) of $x \in \mathbb{H}$ with respect to P_X is defined as

$$D_\beta(x; P_X) = \inf_{v \in \mathcal{V}_\beta} (1 + O_v(x; P_X))^{-1}, \quad (3)$$

where the projection outlyingness O_v is given in (1).

The previous study **[B]** focused on the theoretical properties of **RPD**. In particular, the non-degeneracy of **RPD** is established, meaning that for $\beta > 0$, the depth function $D_\beta(\cdot; P_X)$ is strictly positive. Further, it is shown that **RPD** preserves several properties of the usual multivariate projection depth, including quasiconcavity and monotonicity, and is well-behaved under symmetry. Moreover, it exhibits other desirable properties: it is invariant under orthogonal transformations and shifts; for $\beta > 0$, **RPD** is $1/\beta$ -Lipschitz,

¹We define the median of a real-valued random variable U , denoted by $\text{med}[U]$, as the midpoint of all values $m \in \mathbb{R}$ satisfying $\min\{\mathbb{P}(U \leq m), \mathbb{P}(U \geq m)\} \geq \frac{1}{2}$. The median absolute deviation $\text{MAD}[U]$ is then defined as $\text{med}[|U - \text{med}[U]|]$.

hence continuous. Under mild conditions, it also satisfies the vanishing-at-infinity property. Importantly, uniform consistency of the sample **RPD** on bounded sets is established, and a high breakdown point of the induced median (any point in \mathbb{H} that maximizes **RPD**) is proved. Nevertheless, the practical performance and applicability of **RPD** remain largely unexplored, although [B, Section 4] provides a brief simulation study on outlier detection as a proof of concept.

The primary goal of this paper is to explore practical aspects of the **RPD**. We suggest selecting the regularization parameter β in the **RPD** definition as a quantile with level $u \in (0, 1)$ of the randomly drawn projections. Importantly, we show that this choice preserves key theoretical properties of the **RPD**, including non-degeneracy and consistency. Using a quantile-based β also enhances data adaptivity; for instance, smaller values of u help highlight shape features in functional data. In practice, this selection can be implemented through the random projection approximation used for computing the **RPD**, whose theoretical validity is established.

Building on these foundations, we next conduct extensive numerical studies across several important statistical tasks for functional data analysis. Compared with statistical methods based on widely used functional depths, the **RPD** demonstrates strong overall statistical performance. Its advantages are especially pronounced when shape features play a central role: in such settings, it clearly outperforms existing depths. For example, the **RPD** can nearly perfectly detect functional data exhibiting shape differences, whereas other depths show almost no effectiveness for these complex cases, underscoring its practical value.

The remainder of the paper is organized as follows. Section 2 proposes a strategy for selecting the regularization parameter and examines which theoretical results of [B] continue to hold when that parameter is taken in a data-adaptive manner. In Section 3, we describe an efficient and simple method for approximate computation of the (sample) **RPD**, establish the consistency of this approximation, and analyze its convergence properties. Our statistical contributions are provided in Section 4, which mainly addresses four tasks: (i) outlier detection (Section 4.1), (ii) supervised classification (Section 4.2), (iii) hypothesis testing (Section 4.3), and (iv) robust location estimation (Section 4.4). For each task, we demonstrate the applicability of **RPD** and evaluate its performance relative to other, both classical and cutting-edge depth notions across a variety of scenarios. Proofs of all theoretical results are given in Appendix A, while Appendix B contains supplements to simulation studies performed in Section 4.

Notations

We consider a separable (typically infinite-dimensional) Hilbert space \mathbb{H} with inner product $\langle \cdot, \cdot \rangle$ and the induced norm $\|\cdot\|$. Let $\mathbb{S} = \{v \in \mathbb{H} : \|v\| = 1\}$ denote the unit sphere in \mathbb{H} . For a set $A \subseteq \mathbb{H}$, we use $\text{cl}(A)$ and $\text{span}(A)$ to denote the closure and linear span of A , respectively. All random variables are defined on a common probability space $(\Omega, \mathcal{F}, \mathbb{P})$. Throughout the paper, “a.s.” stands for “almost surely.” The set of all Borel probability measures on a metric space \mathbb{M} is denoted by $\mathcal{P}(\mathbb{M})$; we write $X \sim P_X \in \mathcal{P}(\mathbb{M})$ for a random variable X in \mathbb{M} whose distribution is P_X . The symbol $\stackrel{d}{=}$ denotes equality in distribution.

$Z_n \xrightarrow[n \rightarrow \infty]{\text{a.s.}} Z$ denotes convergence almost surely (a.s.) of random variables $\{Z_n\}_{n=1}^\infty$ to Z as $n \rightarrow \infty$.

2. Selection of tuning parameter

The previous study [B] developed the theory of the **RPD** under the assumption of a fixed parameter $\beta > 0$. In practice, however, the parameter β is taken as the u -quantile of $\text{MAD}[\langle X, V \rangle]$, where V is independent of X and supported on \mathbb{S} ; see also [B, Section 4]. Formally, we make the following definition.

Definition (Regularization based on quantiles). Let $u \in [0, 1)$ and let V be a random element whose support is the whole set \mathbb{S} .² Consider the univariate random variable

$$\text{MAD}[\langle X, V \rangle](\omega) = \text{MAD}[\langle X, V(\omega) \rangle], \quad \omega \in \Omega,$$

and define

$$\beta(u) = q_u[\text{MAD}[\langle X, V \rangle]] \quad (4)$$

be the u -quantile³ of $\text{MAD}[\langle X, V \rangle]$. Note that we treat $\text{MAD}[\langle X, V \rangle]$ in (4) as a random variable with respect to the random element V (considering X as fixed), and therefore, when computing quantiles, we take into account the randomness induced by V . We will adhere to this convention throughout the paper, whenever writing $\text{MAD}[\langle X, V \rangle]$. Using $\beta(u)$, we set

$$\mathcal{V}_{(u)} = \mathcal{V}_{\beta(u)} \quad \text{and} \quad D_{(u)}(\cdot; P_X) = D_{\beta(u)}(\cdot; P_X). \quad (5)$$

The depth $D_{(u)}$ is the **RPD** based on a regularization by the u -quantile of $\text{MAD}[\langle X, V \rangle]$ that is used in practice. Intuitively, in (5) we restrict attention to the $(1 - u)$ -fraction of directions $v \in \mathbb{S}$ with the largest values of $\text{MAD}[\langle X, v \rangle]$ in (2). Smaller values of u correspond to weaker regularization, with $\mathcal{V}_{(0)} = \mathbb{S}$ in the boundary case. Note that the regularization in the definition of **RPD** can be viewed as a form of effective dimension reduction. Choosing the regularization parameter $\beta(u)$ as a quantile therefore allows us to quantify the degree of effective dimension reduction by means of a scalar $u \in [0, 1)$.

The choice of β as a u -quantile guarantees that $\mathcal{V}_{(u)} \neq \emptyset$, see [B, Theorem 3]. As shown in the following result, for $u > 0$, we obtain that $\beta(u) > 0$ under mild assumptions. Recall that a hyperplane in \mathbb{H} is a set of the form $\{x \in \mathbb{H} : \langle x, v \rangle = c\}$ for some $v \in \mathbb{S}$ and $c \in \mathbb{R}$.

Lemma 1. *Let $X \sim P_X \in \mathcal{P}(\mathbb{H})$ and consider $u \in (0, 1)$. Suppose that $V \sim \nu \in \mathcal{P}(\mathbb{S})$ is smooth in the sense that $\nu(H) = 0$ for every hyperplane $H \subset \mathbb{H}$ passing through the origin. If P_X has no atom with probability at least $1/2$, i.e.*

$$\sup_{x \in \mathbb{H}} P_X(\{x\}) < \frac{1}{2}, \quad (6)$$

then $\beta(u) > 0$.

²By the support of a random element V we mean the smallest closed set $A \subseteq \mathbb{H}$ such that $\mathbb{P}(V \in A) = 1$.

³Let Z be a non-negative real-valued random variable with distribution function F . The u -quantile of Z is defined as $q_u = \inf \{x \geq 0 : F(x) \geq u\}$. In particular, we define $q_0 = 0$.

The proof of Lemma 1, as well as all the other proofs from this paper, is in Appendix [Appendix A](#). Throughout this paper, we assume that the conditions of Lemma 1 are satisfied. These assumptions are natural, since one may choose ν as the distribution of $Y/\|Y\|$, where Y is (any) centered, non-degenerate Gaussian element in \mathbb{H} . Moreover, assumption (6) on P_X is standard and is typically satisfied.

Note that the choice of the regularization parameter as a quantile does not alter most of the main theoretical results of [\[B\]](#). The differences from the theory developed in [\[B\]](#) are summarized below:

- **Non-degeneracy.** The non-degeneracy of the **RPD** from [\[B, Theorem 2\]](#) holds provided that $u \in [0, 1)$ is such that $\beta(u) > 0$. Lemma 1 above shows that this is satisfied for $u > 0$ under mild assumptions.
- **Orthogonal invariance.** The orthogonal invariance property of the **RPD** from [\[B, Theorem 5\]](#) no longer holds. Let $\mathcal{S}: \mathbb{H} \rightarrow \mathbb{H}$ be a unitary operator,⁴ then the random variable $\text{MAD}[\langle \mathcal{S}X, V \rangle](\omega) = \text{MAD}[\langle X, \mathcal{S}^*V \rangle](\omega)$ has a different distribution from $\text{MAD}[\langle X, V \rangle](\omega)$. Consequently, a unitary transformation \mathcal{S} leads to a different value of $\beta(u)$. A natural idea is to consider V that is unitarily invariant, i.e., $\mathcal{S}V \stackrel{d}{=} V$ for all unitary \mathcal{S} . Unitarily invariant non-degenerate distributions, however, do not exist when $\dim(\mathbb{H}) = \infty$ ([Kuo, 1975](#), p. 1). In practical implementation, nevertheless, this issue does not arise, since the observed functions are represented in a discretized form with finitely many values. Hence, the dimension is finite, and in practice, V is naturally chosen uniformly on the unit sphere of the corresponding finite-dimensional space.
- **Consistency.** The quantile $\beta(u)$ depends on the underlying distribution P_X . Hence, it must be approximated from a random sample. The sample version consistency of **RPD** remains to hold under mild assumptions; we elaborate on this in [Theorem 3](#) in [Section 2.1](#) below.
- **Robustness of the induced median.** [Theorem 10](#) in [\[B\]](#) shows that for fixed $\beta > 0$, the breakdown point of the median induced by the **RPD** equals $1/2$. The case where $\beta = \beta(u)$ is chosen as in [\(4\)](#) is discussed in [Theorem 4](#) in [Section 2.2](#) below.

2.1. Consistency with β chosen as a quantile

For $X \sim P_X \in \mathcal{P}(\mathbb{H})$, consider a random sample $\{X_i\}_{i=1}^n$ of size n , where $X_i \stackrel{d}{=} X$. Denote by \widehat{P}_n the corresponding empirical distribution, $\widehat{P}_n = n^{-1} \sum_{i=1}^n \delta_{X_i}$, where δ_x is the Dirac measure at $x \in \mathbb{H}$. For $v \in \mathbb{S}$, define $\widehat{\text{med}}[\{\langle X_i, v \rangle\}_{i=1}^n]$ and $\widehat{\text{MAD}}[\{\langle X_i, v \rangle\}_{i=1}^n]$ as the

⁴A bounded linear operator $\mathcal{S}: \mathbb{H} \rightarrow \mathbb{H}$ is called *unitary* if and only if $\mathcal{S}\mathcal{S}^* = \mathcal{S}^*\mathcal{S} = \mathcal{I}$, where \mathcal{I} denotes the identity operator and \mathcal{S}^* the adjoint operator of \mathcal{S} .

sample median and sample MAD based on the projections $\{\langle X_i, v \rangle\}_{i=1}^n$, respectively.⁵

With this notation, the regularization parameter $\beta(u)$ is estimated by its sample analogue, that is, we define $\widehat{\beta}_n(u)$ as the u -quantile of $\widehat{\text{MAD}}[\{\langle X_i, V \rangle\}_{i=1}^n]$. Note that this quantile is taken conditionally on $\{X_i\}_{i=1}^n$, thus $\widehat{\beta}_n(u)$ remains random since it depends on the realization of the sample $\{X_i\}_{i=1}^n$. As shown in the following lemma, under mild assumptions, $\widehat{\beta}_n(u)$ is a consistent estimator of $\beta(u)$.

Lemma 2. *Let $X \sim P_X \in \mathcal{P}(\mathbb{H})$ have a contiguous support.⁶ Further assume that $\beta(u)$ is a point of continuity of the distribution function of $\text{MAD}[\langle X, V \rangle]$. Then $\widehat{\beta}_n(u) \xrightarrow[n \rightarrow \infty]{a.s.} \beta(u)$.*

The sample version of the **RPD** is defined as

$$D_{(u)}(x; \widehat{P}_n) = \inf_{v \in \widehat{\mathcal{V}}_{n(u)}} \left(1 + O_v(x; \widehat{P}_n)\right)^{-1} = \left(1 + \sup_{v \in \widehat{\mathcal{V}}_{n(u)}} \frac{|\langle x, v \rangle - \widehat{\text{med}}[\{\langle X_i, v \rangle\}_{i=1}^n]|}{\widehat{\text{MAD}}[\{\langle X_i, v \rangle\}_{i=1}^n]}\right)^{-1}, \quad (7)$$

where

$$\widehat{\mathcal{V}}_{n(u)} = \left\{v \in \mathbb{S} : \widehat{\text{MAD}}[\{\langle X_i, v \rangle\}_{i=1}^n] \geq \widehat{\beta}_n(u)\right\}.$$

Next, we show that defining $\beta(u)$ as a quantile does not affect the consistency of **RPD**, as established in [B, Theorem 7]. To this end, we introduce the maximal outlyingness function Γ_x at $x \in \mathbb{H}$ over \mathcal{V}_t as

$$\Gamma_x(t) = \sup_{v \in \mathcal{V}_t} O_v(x; P_X), \quad t \in [0, \infty). \quad (8)$$

Theorem 3. *Suppose that $X \sim P_X \in \mathcal{P}(\mathbb{H})$ has contiguous support and let $u \in [0, 1)$ be such that $\beta(u) > 0$. Assume that $\beta(u)$ is a point of continuity of the distribution function of $\text{MAD}[\langle X, V \rangle]$. Furthermore, assume that $\mathcal{F} \subset \mathbb{H}$ is a bounded set for which the family $\{\Gamma_x : x \in \mathcal{F}\}$ of maximal outlyingness functions (8) is equicontinuous at β , i.e.,*

$$\limsup_{t \rightarrow \beta} \sup_{x \in \mathcal{F}} |\Gamma_x(t) - \Gamma_x(\beta)| = 0. \quad (9)$$

Then, the sample **RPD** in (7) is uniformly consistent for the population **RPD** in (5) over \mathcal{F} , namely

$$\sup_{x \in \mathcal{F}} \left|D_{(u)}(x; \widehat{P}_n) - D_{(u)}(x; P_X)\right| \xrightarrow[n \rightarrow \infty]{a.s.} 0.$$

⁵For a sample $\{Z_i\}_{i=1}^n \subset \mathbb{R}$ with order statistics $Z_{(1)} < \dots < Z_{(n)}$, the sample median is defined as $\widehat{\text{med}}[\{Z_i\}_{i=1}^n] = Z_{((n+1)/2)}$ if n is odd and $\widehat{\text{med}}[\{Z_i\}_{i=1}^n] = (Z_{(n/2)} + Z_{(n/2+1)})/2$ otherwise. The sample MAD is then defined by $\widehat{\text{MAD}}[\{Z_i\}_{i=1}^n] = \widehat{\text{med}}\left[\left\{\left|Z_i - \widehat{\text{med}}[\{Z_j\}_{j=1}^n]\right|\right\}_{i=1}^n\right]$.

⁶We say that a random variable $X \sim P_X \in \mathcal{P}(\mathbb{H})$ has contiguous support (Kong and Zuo, 2010) if for each $v \in \mathbb{S}$, the support of the real random variable $\langle X, v \rangle$ is connected.

Theorem 3 states that the consistency of the sample version $D_{(u)}(\cdot, \widehat{P}_n)$ is essentially equivalent to condition (9), that is, to the uniform continuity of the maximal outlyingness function $\Gamma_x(\cdot)$. This continuity is, in fact, required already for the consistency of the standard **RPD** with a fixed parameter β , as expounded in [B, Theorem 7]. It can be shown that (9) is satisfied, for instance, in the case of elliptically symmetric distributions [B, Theorems 8 and 9].

2.2. Robustness of the induced median with β chosen as a quantile

Robustness analysis plays a central role in the study of depth-based functionals. An estimator is said to be robust if small perturbations in the data distribution do not lead to substantial changes in its value. We assess robustness through the breakdown point, which represents the maximum fraction of contamination that can be introduced before the estimator becomes arbitrarily unreliable. The breakdown point is a crucial measure of the robustness of any statistical functional (Huber and Ronchetti, 2009).

Here, let $X \sim P_X \in \mathcal{P}(\mathbb{H})$ and $u \in (0, 1)$. Recall that in [B], the **RPD** median of P_X is defined as

$$\theta(P_X) = \theta_{(u)}(P_X) = \operatorname{argmax} \{D_{(u)}(\theta; P_X) : \theta \in \operatorname{cl}(\operatorname{span}(\mathcal{V}_{(u)}))\}. \quad (10)$$

The reason for considering only points $\theta \in \operatorname{cl}(\operatorname{span}(\mathcal{V}_{(u)}))$ is that all relevant information about P_X in $D_{(u)}(\cdot; P_X)$ is contained in this subspace. More precisely, [B, Theorem 5d] shows that $D_{(u)}(x; P_X) = D_{(u)}(\widehat{x}; P_X)$ for any $x \in \mathbb{H}$ and its orthogonal projection \widehat{x} onto $\operatorname{cl}(\operatorname{span}(\mathcal{V}_{(u)}))$.

Assume that $V \sim \nu \in \mathcal{P}(\mathbb{S})$ is smooth and that P_X has no atoms. For $\varepsilon \in [0, 1]$ and $Q \in \mathcal{P}(\mathbb{H})$, define the ε -contaminated distribution $P_{(Q, \varepsilon)} \in \mathcal{P}(\mathbb{H})$ as

$$P_{(Q, \varepsilon)}(A) = (1 - \varepsilon)P_X(A) + \varepsilon Q(A), \quad \text{for all Borel sets } A \subseteq \mathbb{H}.$$

Let $\beta(u)$ denote the regularization parameter for P_X , and let $\beta_{(Q, \varepsilon)}(u)$ be the corresponding parameter for $P_{(Q, \varepsilon)}$, defined as the u -quantile of

$$\operatorname{MAD}[\langle X', V \rangle], \quad \text{where } X' \sim P_{(Q, \varepsilon)}.$$

Under our assumptions, Lemma 1 ensures that $\beta(u) > 0$, and for $\varepsilon < 1/2$ we also have $\beta_{(Q, \varepsilon)}(u) > 0$ for any $Q \in \mathcal{P}(\mathbb{H})$.

The direction set $\mathcal{V}_{(u)}$ is associated with P_X . Its contaminated counterpart $\mathcal{V}_{(u)}(Q, \varepsilon)$ is defined by

$$\mathcal{V}_{(u)}(Q, \varepsilon) = \{v \in \mathbb{S} : \operatorname{MAD}[\langle X', v \rangle] \geq \beta_{(Q, \varepsilon)}(u)\}, \quad \text{where } X' \sim P_{(Q, \varepsilon)}.$$

By construction, since $\beta(u)$ is defined as a u -quantile, both $\mathcal{V}_{(u)}$ and $\mathcal{V}_{(u)}(Q, \varepsilon)$ are non-empty for all $Q \in \mathcal{P}(\mathbb{H})$.

As opposed to the classical notion of a breakdown point (Huber and Ronchetti, 2009), we consider a slightly modified version of the breakdown point tailored to our infinite-dimensional setup. The breakdown point of the **RPD** median $\theta = \theta(P_X)$ of P_X is defined

as⁷

$$\varepsilon_{(u)}^*(\theta; P_X) = \inf \left\{ \varepsilon \in [0, 1] : \sup_{Q \in \mathcal{P}(\mathbb{H})} \sup_{v \in \mathcal{V}_{(u)}(Q, \varepsilon)} |\langle \theta(P_{(Q, \varepsilon)}) - \theta(P_X), v \rangle| = \infty \right\}. \quad (11)$$

In contrast to the classical definition, the distance $\|\theta(P_{(Q, \varepsilon)}) - \theta(P_X)\|$ used in the classical breakdown point is replaced in (11) by the maximum inner product. This is quite natural in our setup. On one hand, the Cauchy-Schwarz inequality (Dudley, 2002, Theorem 5.3.3) gives

$$\sup_{v \in \mathbb{S}} |\langle \theta(P_{(Q, \varepsilon)}) - \theta(P_X), v \rangle| = \|\theta(P_{(Q, \varepsilon)}) - \theta(P_X)\|, \quad (12)$$

while on the other hand, in the definition of the **RPD** median in (10) we restrict ourselves only to the regularized directions in the linear span of $\mathcal{V}_{(u)}$. For that reason, the supremum over $v \in \mathbb{S}$ in (12) is replaced by the weaker supremum over $v \in \mathcal{V}_{(u)}(Q, \varepsilon)$ in (11).

The breakdown point analysis for the **RPD** median with $\beta(u)$ chosen as a quantile depends on the smoothness of both P_X and $V \sim \nu$. Let F_v denote the distribution function of $\langle X, v \rangle$ for $v \in \mathbb{S}$, and define its modulus of continuity

$$\omega_v(\delta) = \sup_{|t_1 - t_2| \leq \delta} |F_v(t_1) - F_v(t_2)|, \quad \delta \geq 0.$$

For $\varepsilon \in (0, 1/2)$, consider the technical condition

$$\exists \gamma > 0 : \nu \left(\left\{ v \in \mathbb{S} : \omega_v(\gamma) < \frac{1/2 - \varepsilon}{1 - \varepsilon} \right\} \right) \geq 1 - u. \quad (13)$$

This condition essentially states that there exist sufficiently many directions $v \in \mathbb{S}$ (in terms of the measure ν) for which the projection $\langle X, v \rangle$ is sufficiently scattered. Note that the function $\omega_v(\cdot)$ is non-decreasing. Consequently, if (13) holds for some γ , it also holds for all $0 < \gamma' \leq \gamma$.

Theorem 4. *Consider $X \sim P_X \in \mathcal{P}(\mathbb{H})$ with no atoms, $u \in (0, 1)$, and assume that $V \sim \nu \in \mathcal{P}(\mathbb{S})$ is smooth. If assumption (13) holds for some $\varepsilon \in (0, 1/2)$, then*

$$\sup_{Q \in \mathcal{P}(\mathbb{H})} \sup_{v \in \mathcal{V}_{(u)}(Q, \varepsilon)} |\langle \theta(P_{(Q, \varepsilon)}) - \theta(P_X), v \rangle| < \infty.$$

Consequently, if (13) holds for every $\varepsilon \in (0, 1/2)$, then $\varepsilon_{(u)}^(\theta; P_X) = 1/2$.*

This result is remarkable, as it shows that under quite mild conditions, the infinite-dimensional **RPD** median achieves the highest possible breakdown point of $1/2$, attainable by location-equivariant estimators (Huber and Ronchetti, 2009).

⁷Since $\mathcal{V}_{(u)} \neq \emptyset$ and $\mathcal{V}_{(u)}(Q, \varepsilon) \neq \emptyset$, the sets of medians $\mathfrak{M}(P_X)$ and $\mathfrak{M}(P_{(Q, \varepsilon)})$ are non-empty, see [B, Theorem 6]. The particular choice of representatives $\theta(P_X)$ and $\theta(P_{(Q, \varepsilon)})$ does not affect our results.

A natural question is when the technical condition (13) holds. Consider, for instance, the case of Gaussian distributions in \mathbb{H} . That is, assume that X has a centered Gaussian distribution with a positive definite covariance operator $\Sigma: \mathbb{H} \rightarrow \mathbb{H}$ (Hsing and Eubank, 2015, Definition 7.2.3). This implies that for any $v \in \mathbb{S}$, the random variable $\langle X, v \rangle$ follows a univariate Gaussian distribution with zero mean and variance $\langle v, \Sigma v \rangle$. In this setting, we can bound the modulus of continuity

$$\omega_v(\delta) = \sup_{|t_1 - t_2| \leq \delta} |F_v(t_1) - F_v(t_2)| \leq \delta \sup_{t \in \mathbb{R}} f_v(t) \leq \frac{\delta}{\sqrt{2\pi \langle v, \Sigma v \rangle}},$$

where f_v denotes the probability density function of $\langle X, v \rangle$. It follows that if there exists $\gamma > 0$ such that

$$\begin{aligned} \nu \left(\left\{ v \in \mathbb{S} : \omega_v(\gamma) < \frac{1/2 - \varepsilon}{1 - \varepsilon} \right\} \right) &\geq \nu \left(\left\{ v \in \mathbb{S} : \frac{\gamma}{\sqrt{2\pi \langle v, \Sigma v \rangle}} < \frac{1/2 - \varepsilon}{1 - \varepsilon} \right\} \right) \\ &= \nu \left(\left\{ v \in \mathbb{S} : \langle v, \Sigma v \rangle > \left(\frac{(1 - \varepsilon)\gamma}{(1/2 - \varepsilon)\sqrt{2\pi}} \right)^2 \right\} \right) \geq 1 - u, \end{aligned} \quad (14)$$

then (13) is satisfied. Moreover, note that for $V \sim \nu$, the random variable $\langle V, \Sigma V \rangle(\omega) = \langle V(\omega), \Sigma V(\omega) \rangle$, $\omega \in \Omega$, is strictly positive. Consequently, the u -quantile of $\langle V, \Sigma V \rangle$, for any $u > 0$, is always positive, implying that for any $\varepsilon \in (0, 1/2)$, there exists a $\gamma > 0$ such that (14) holds. Theorem 4 then implies that $\varepsilon_{(u)}^*(\theta; P_X) = 1/2$ for any Gaussian distribution P_X with a positive definite covariance operator. The same argument applies to elliptically symmetric distributions in \mathbb{H} (Boente et al., 2014) with a positive definite scatter operator, for which all projections $\langle X, v \rangle$, $v \in \mathbb{S}$, possess bounded densities.

Note that the condition (13) is more strict for smaller values of $u > 0$. This indicates that stronger regularization leads to more robust estimators of location. This will be illustrated in our numerical examples in Section 4.4.

3. Computation of RPD

The definition of the **RPD** in (3) requires computing an infimum over the set of directions $\mathcal{V}_{(u)} \subseteq \mathbb{S}$. Although the **RPD** can be interpreted as a conditional version of the classical projection depth (Zuo, 2003), directly computing this infimum in a potentially infinite-dimensional Hilbert space \mathbb{H} poses a significant challenge. While sophisticated algorithms exist for projection depth in finite-dimensional settings (e.g., Liu and Zuo, 2014; Shao et al., 2022), they do not scale well to functional data.

To address this issue, we employ a stochastic approximation algorithm inspired by Dyckerhoff (2004, Section 6). Instead of evaluating the infimum over the entire set $\mathcal{V}_{(u)}$, we minimize the outlyingness over a finite set of directions drawn independently from a probability distribution supported on $\mathcal{V}_{(u)}$. Since $\mathcal{V}_{(u)} = \mathcal{V}_{\beta(u)}$, we must first estimate the quantile $\beta(u)$. To this end, we sample $\{u_1, \dots, u_L\} \in \mathbb{S}$, $L \in \mathbb{N}$ independent directions from ν and compute $\beta^{(L)}(u)$ as the sample u -quantile of $\{\text{MAD}[\langle X, u_i \rangle]\}_{i=1}^L$. Subsequently, we sample

$M \in \mathbb{N}$ independent directions $\{v_1, \dots, v_M\} \in \mathbb{S}$ from the distribution ν conditioned on $\mathcal{V}_{(u)}^{(L)} = \mathcal{V}_{\beta^{(L)}(u)}$. The approximated random **RPD** is then defined as

$$D_{(u)}^{(M)}(x; P_X) = \min_{m=1, \dots, M} (1 + O_{v_m}(x; P_X))^{-1}. \quad (15)$$

This approach reduces the complex optimization problem to a straightforward evaluation of univariate outlyingness functions. The validity of this approximation is ensured by the following consistency result.

Theorem 5 (Consistency of the random **RPD**). *Consider $x \in \mathbb{H}$ and $P_X \in \mathcal{P}(\mathbb{H})$ with either finite or contiguous support. Let $\nu \in \mathcal{P}(\mathbb{S})$ be such that its support is the whole set \mathbb{S} . Assume that $\beta(u)$ in (4) is uniquely defined, i.e., the distribution function of $\text{MAD}[\langle X, V \rangle]$ is strictly increasing at $\beta(u)$. Additionally, assume that $\Gamma_x(\cdot)$ in (8) is continuous at $\beta(u)$. Then, the approximated random **RPD** (15) converges almost surely to the theoretical **RPD** as the number of directions increases:*

$$\lim_{M, L \rightarrow \infty} D_{(u)}^{(M)}(x; P_X) = D_{(u)}(x; P_X) \quad a.s.$$

For practical implementation, we leverage the computational efficiency of C++ integrated into the R environment via the RcppArmadillo package (Eddelbuettel et al., 2024). The algorithm corresponding to (15) is available in the software package RPD.⁸

The choice of the numbers of directions L and M presents a trade-off between computational efficiency and approximation accuracy. While larger values improve the quality of the approximation, they also increase the computational cost. This issue becomes particularly pronounced for functional data with high effective dimensionality, which may make the stochastic approximation computationally intensive. Consequently, the main drawback of the **RPD** is that in practice, it is computed approximately. Unless stated otherwise, in all subsequent computations we set $L = 1\,000$ and $M = 10\,000$. These choices ensure that, even for datasets of moderate size (in the order of several thousand observations) and moderate discretization resolution (around 100 grid points), the resulting computations can be performed within a few seconds.

In practice, the approximation of the regularization parameter $\beta^{(L)}(u)$ is less critical than the approximation of the depth itself. Therefore, it is generally more important to choose a sufficiently large value of M to ensure an accurate evaluation of the **RPD**.

Figure 1 illustrates the convergence behavior of the stochastic approximation for representative functional observations. Empirical evidence indicates that the stochastic approximation converges more rapidly for outlying functions than for more central ones. This phenomenon can be attributed to the fact that, for outliers, it is typically easier to identify a projection direction in which the function appears extreme, whereas for more central functions the search for the most extreme direction is inherently more challenging.

⁸Available online at <https://github.com/NagyStanislav/RPD>.

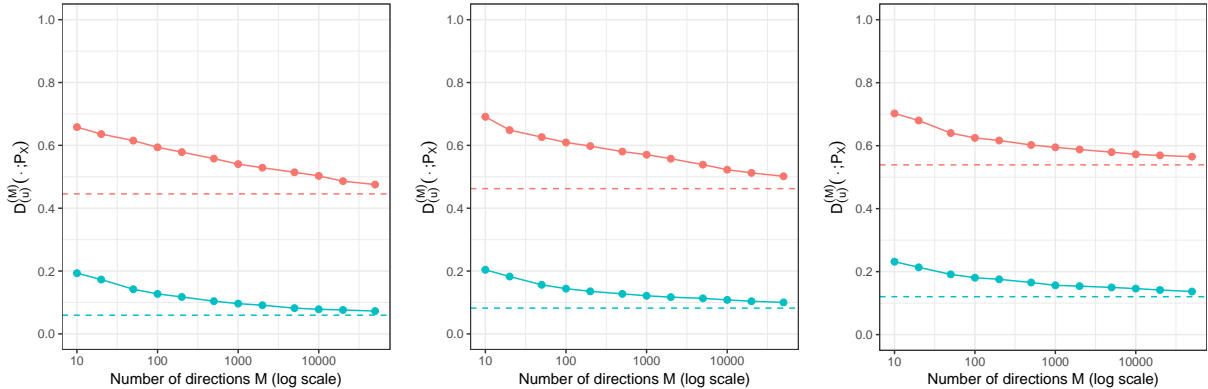


Figure 1: Convergence rate plots of $D_{(u)}^{(M)}$ with $u = 0.001$ (left), $u = 0.1$ (middle), and $u = 0.5$ (right). The depth is evaluated for a central function $x(t) = 0$, $t \in [0, 1]$ (red), and for a peripheral function $x(t) = 1.5 \sin(2\pi t)$, $t \in [0, 1]$ (blue). The reference dataset consists of $n = 50$ independent centered Gaussian trajectories with covariance function $\Sigma(s, t) = \exp(-(s - t)^2/0.32)$, discretized on a grid of $T = 51$ points. The plots show $D_{(u)}^{(M)}(x; \hat{\mathbb{P}}_n)$ as a function of M , averaged over 20 Monte Carlo simulations, with dashed horizontal lines corresponding to $M = 10^7$. The stochastic approximation of **RPD** converges substantially more slowly for central functions than for peripheral ones.

A closely related phenomenon was studied by [Briand et al. \(2025\)](#) in the context of the random approximation of the classical multivariate halfspace (Tukey) depth. The authors show that, for points whose depth is bounded away from both 0 and $1/2$, the random halfspace depth provides an inefficient approximation of the exact halfspace depth. An analogous effect is observed in the present setting for the randomized **RPD**.

4. Simulations

We assess the practical utility of **RPD** in four statistical tasks: (i) outlier detection, (ii) supervised classification, (iii) hypothesis testing for the equality of two distributions, and (iv) robust location estimation. We compare **RPD** with the following functional depths:

- **RHD**: the regularized halfspace depth ([Yeon et al., 2025](#)) with a relatively high and fixed dimension $J = 6$. This choice is motivated by the simulation results reported in [\[B\]](#), where **RHD** with $J = 6$ was observed to perform better. We also considered the default choice of J , which led to inferior performance, and is therefore not reported here;
- **FD**: the integrated halfspace depth ([Fraiman and Muniz, 2001](#); [Nagy et al., 2016](#));
- **MBD**: the modified band depth ([López-Pintado and Romo, 2009](#));
- **ID**: the infimal halfspace depth ([Mosler, 2013](#)), representing infimal/extremal depths from the literature ([Narisetty and Nair, 2016](#)); and

- **SD**: the spherical depth (Elmore et al., 2006; Mendroš and Nagy, 2025).

All our simulations are performed in the statistical software R. We employ the RPD package for **RPD**, the RHD package for **RHD**,⁹ and dalpha for **FD**, **ID**, **MBD**, and **SD**. For **RPD**, the regularization parameter is chosen based on the u -quantile as defined in (4), and to ensure consistency with the definition used in this paper, we use the $(1 - u)$ -quantile for **RHD**. This will be denoted as **RPD** _{u} and **RHD** _{u} . Several values of u are considered and their impact is discussed.

We consider the separable Hilbert space $\mathbb{H} = L_2([0, 1])$ of square-integrable functions on $[0, 1]$, equipped with the standard inner product $\langle x, y \rangle = \int_0^1 x(t)y(t) dt$ and the induced norm $\|x\| = \sqrt{\int_0^1 x(t)^2 dt}$ for $x, y \in \mathbb{H}$. In practice, each function $x \in \mathbb{H}$ is observed on a discrete grid of $T = 101$ equidistant points $t_1, \dots, t_T \in [0, 1]$, so that the L_2 -norm is approximated by its discrete counterpart $\|x\| \approx \sqrt{\sum_{k=1}^T x(t_k)^2 / T}$.

4.1. Outlier detection

For the outlier detection task, we consider $n = 500$ independent random functions $\{X_i(t)\}_{i=1}^n$, $t \in [0, 1]$, among which $m = 50$ are outliers. This corresponds to a contamination level of $\varepsilon = 0.1$. To provide a comprehensive evaluation, we consider a wide spectrum of different types of functional outliers, including magnitude, phase, shape, covariance, and frequency anomalies. In these models, $\{e_i(t)\}_{i=1}^n$ are independent errors taken as realizations of centered Gaussian processes with covariance function $\Sigma(s, t) = \lambda \exp(-|s - t|/\lambda)$ for $s, t \in [0, 1]$, for some $\lambda > 0$. We study the following data-generating processes:

Model (D₁) *Magnitude outliers*: The non-contaminated observations are generated according to $X_i(t) = 4t + e_i(t)$, $t \in [0, 1]$, where $e_i(t)$ is taken with $\lambda = 1$. The outlying observations follow the model $X_i(t) = 4t + 8k_i + e_i(t)$, where $k_i \in \{-1, 1\}$ with $\mathbb{P}(k_i = 1) = \mathbb{P}(k_i = -1) = 0.5$.

Model (D₂) *Location difference model*: The clean observations are generated according to $X_i(t) = 30t(1-t)^{1.5} + e_i(t)$, $t \in [0, 1]$, with $\lambda = 0.3$. The outlying observations follow the model $X_i(t) = 30t^{1.5}(1-t) + e_i(t)$.

Model (D₃) *Covariance structure difference model*: The clean observations are $X_i(t) = 4t + e_i(t)$, $t \in [0, 1]$, with $\lambda = 1$. The outlying observations follow the model $X_i(t) = 4t + f_i(t)$, where $\{f_i(t)\}_{i=1}^m$ are independent centered Gaussian processes with covariance function $\Sigma(s, t) = 5 \exp(-2|t - s|^{0.5})$, $s, t \in [0, 1]$.

Model (D₄) *Shifted periodic outliers*: The clean observations are $X_i(t) = 2 \sin(15\pi t) + e_i(t)$, $t \in [0, 1]$, with $\lambda = 1$. The outlying observations are taken as $X_i(t) = 2 \sin(15\pi t + 2) + e_i(t)$.

⁹Available online at <https://github.com/luckyhm1928/RHD>.

Model (D₅) *Central high-frequency outliers*: The clean observations are $X_i(t) = e_i(t)$, $t \in [0, 1]$, with $\lambda = 1$. The outlying observations follow the model $X_i(t) = \sin(20(t+\theta_i)\pi) + f_i(t)$, where $\{\theta_i\}_{i=1}^m$ are independent and uniform on $(0.25, 0.5)$ and $\{f_i(t)\}_{i=1}^m$ are independent centered Gaussian processes with covariance $\Sigma(s, t) = 0.1 \exp(-|t - s|^{0.1}/4)$, $s, t \in [0, 1]$.

Model (D₆) *Central shape outliers*: Take a basis of orthogonal polynomials ϕ_1, \dots, ϕ_6 on $[0, 1]$ of maximum degree 5 (with ϕ_1 denoting the constant function of degree 0, etc.). The non-contaminated observations are generated as $X_i(t) = \sum_{j=1}^6 c_i^j \phi_j(t)$, $t \in [0, 1]$, where $\{c_i\}_{i=1}^n = \{(c_i^1, \dots, c_i^6)^\top\}_{i=1}^n$ are independent centered Gaussian random vectors with covariance matrix $\Sigma \in \mathbb{R}^{6 \times 6}$ having unit diagonal and all off-diagonal elements equal to 0.95. The outlying observations follow the model $X_i(t) = \sum_{j=1}^6 b_i^j \phi_j(t)$, $t \in [0, 1]$, where $\{b_i\}_{i=1}^m = \{(b_i^1, \dots, b_i^6)^\top\}_{i=1}^m$ are independent Gaussian random vectors centered at $(1, 1, \dots, 1)^\top \in \mathbb{R}^6$ with covariance matrix $\Sigma^{-1}/100$.

Models (D₁)–(D₅) were inspired by Cuevas et al. (2007); Arribas-Gil and Romo (2014); Ojo et al. (2022) and Jiménez-Varón et al. (2024). Model (D₆) was used in [B]. Examples of simulated datasets from (D₁)–(D₆) are in Figure B.6 in Appendix B.

To identify outlying functions, functional depths were evaluated on the pooled sample of $n = 500$ functions. The functions were ranked according to their depth, with rank $1/500 \approx 0$ corresponding to the least deep function and rank $500/500 = 1$ to the deepest curve. As a measure of outlier detection performance, we computed the mean rank of the $m = 50$ (true) outliers for each functional depth. The experiment was repeated over 100 independent Monte Carlo runs, and the means and standard deviations (in parentheses) of the resulting mean outlier ranks are reported in Table 1.

Model	RPD _{0.001}	RPD _{0.1}	RHD _{0.001}	RHD _{0.1}	FD	MBD	ID	SD
(D ₁)	0.051 (0.000)	0.051 (0.000)	0.078 (0.008)	0.067 (0.007)	0.051 (0.000)	0.051 (0.000)	0.052 (0.002)	0.052 (0.002)
(D ₂)	0.051 (0.000)	0.051 (0.000)	0.209 (0.016)	0.197 (0.013)	0.064 (0.004)	0.063 (0.004)	0.208 (0.016)	0.214 (0.011)
(D ₃)	0.051 (0.000)	0.051 (0.000)	0.085 (0.011)	0.109 (0.017)	0.185 (0.014)	0.157 (0.012)	0.055 (0.001)	0.056 (0.002)
(D ₄)	0.051 (0.000)	0.051 (0.000)	0.167 (0.013)	0.160 (0.012)	0.129 (0.010)	0.115 (0.009)	0.146 (0.011)	0.118 (0.005)
(D ₅)	0.051 (0.000)	0.054 (0.003)	0.183 (0.027)	0.536 (0.050)	0.513 (0.017)	0.518 (0.017)	0.564 (0.022)	0.361 (0.017)
(D ₆)	0.051 (0.001)	0.062 (0.008)	0.219 (0.066)	0.663 (0.037)	0.704 (0.023)	0.681 (0.023)	0.419 (0.029)	0.613 (0.024)

Table 1: *Outlier detection: Means and standard deviations (in parentheses) of the average rank of the outlying curves; lower values indicate better performance. The smallest average ranks are written in bold. In the ideal case, the 50 curves with the smallest depth values coincide exactly with the outliers, yielding an average outlier rank of $((1 + 50)/2)/500 = 0.051$.*

The results show that **RPD** consistently delivers near-perfect performance across all considered models. In the simple Model (D₁), all depth notions are able to accurately detect the shift in outlying functions. Models (D₂), (D₃), and (D₄) involve location, covariance-structure, and shifted periodic outliers, respectively. These types of outliers are more challenging to identify; however, they still manifest themselves as pointwise vertical deviations,

which explains why the remaining depth notions (not necessarily projection-based) continue to exhibit reasonably good performance. For instance, in Model (D₂), **FD** (and the closely related **MBD**) performs comparably to **RPD**. In Model (D₃), good detection results are obtained by **RHD**, and in particular also by **ID** and **SD**. In contrast, for Model (D₄), all considered depth notions except **RPD** yield an average rank of the outlying curves exceeding 0.11, indicating that the set of lowest-depth curves already contains a substantial number of non-outlying observations. Even at this stage, **RPD** maintains consistently strong performance.

The main strength of **RPD** becomes evident in Models (D₅) and (D₆). In these settings, the outliers tend to remain within the central region of the data cloud while having markedly different shapes. Here, the advantage of **RPD** stems from its projection-based nature, whereas depths such as **FD**, **ID**, or **MBD** rely solely on pointwise vertical deviations and therefore fail to adequately capture such shape outlyingness. The only competing depth that still provides reasonably good performance is **RHD**, and only when using a small regularization parameter $u = 0.001$. In contrast, **RPD** achieves almost perfect results in both models.

For Model (D₆), we observe that **RPD** with regularization parameter $u = 0.1$ performs worse than **RPD** with $u = 0.001$. This behavior is explained by the fact that stronger regularization leads to reduced sensitivity of the depth. Consequently, for the purpose of outlier detection, we generally recommend using a very small value of the regularization parameter u , such as $u = 0.001$, as employed here.

Note that **RHD**, in certain cases, performs worse than classical depth measures such as **FD** and **ID**. This is attributed to the inherently discrete nature of **RHD**, which often produces tied rankings and thus constrains its capacity to differentiate among multiple outlying curves. As a result, **RHD** has been designed with an additional outlier detection procedure (cf. Yeon et al., 2025, Section 3), which may nonetheless be computationally intensive. In contrast, **RPD** provides significant practical advantages, as it allows for direct identification of outliers through small depth values, eliminating the need for any supplementary detection algorithms.

A comparison of the performance of **RPD**, **MBD**, and **SD** under Model (D₅) is shown in Figure 2. While **RPD** successfully detects the central shape outlying curves, both **MBD** and **SD** primarily identify curves located at the periphery of the data cloud as outliers, because they attach more importance to location (horizontal shift) than severe differences in shape.

4.2. Classification

As a next application, we consider the classical binary supervised classification task. In each of the three considered models, we sample $n = 500$ functions independently from each of the two groups given by X and Y , respectively:

Model (C₁) *Location difference model:* X and Y are Gaussian processes with mean functions $\mu_X(t) = 30t^{1.2}(1-t)$ and $\mu_Y(t) = 30t(1-t)^{1.2}$, respectively, both with covariance $\Sigma(s, t) = 0.2 \exp(-|s-t|/0.3)$, $s, t \in [0, 1]$. This is the standard location-difference model from Cuevas et al. (2007); see also the left-hand panel of Figure 3. This model is a slight modification of (D₂).

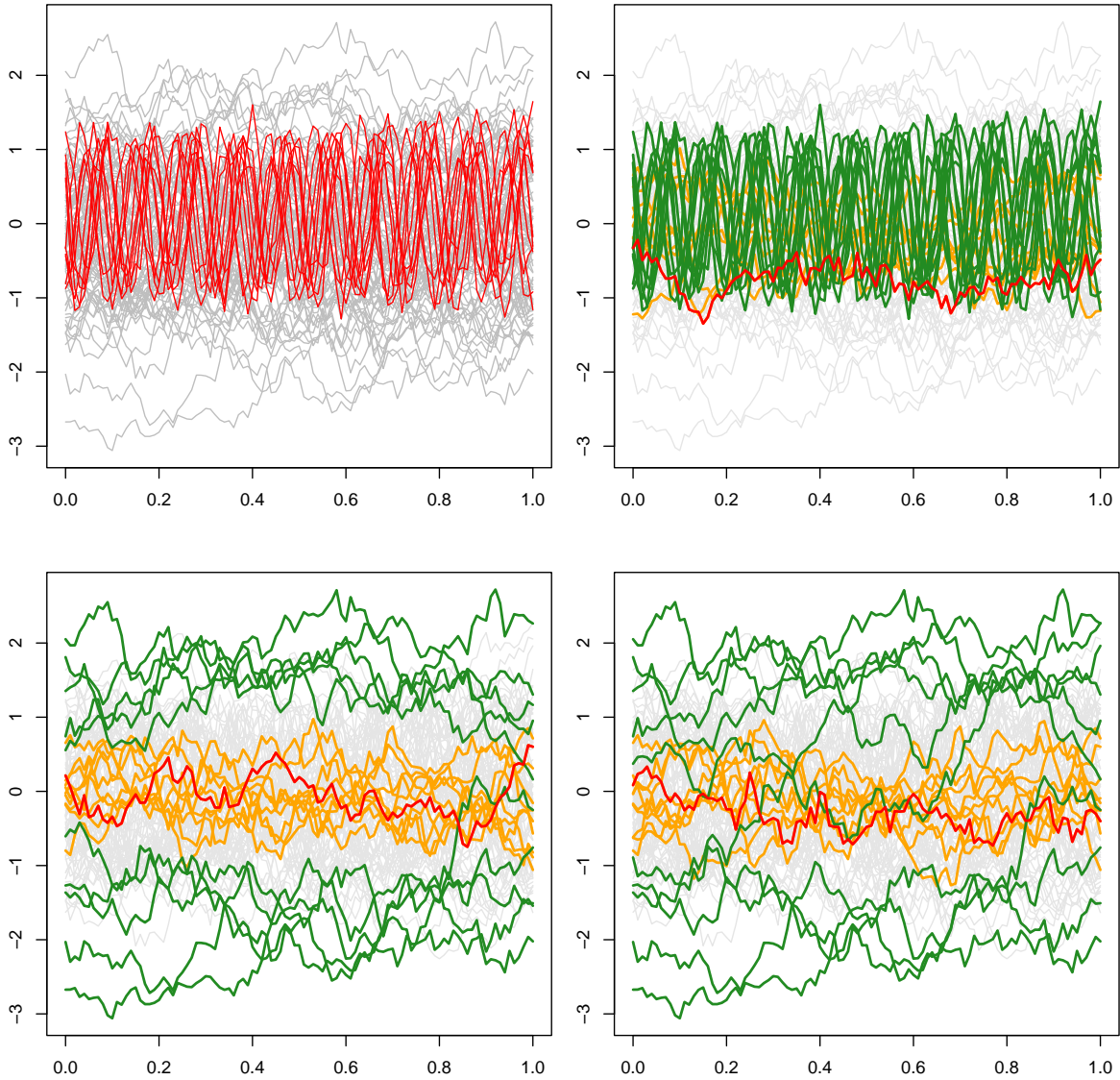


Figure 2: A single random sample of functional observations (gray) generated from Model (D_5) with sample size $n = 100$, containing $m = 10$ outlying curves (red) (top left). The same sample is shown with the sample median curve highlighted in red, the 10% deepest observations in orange, and the 10% least deep observations in green, based on **RPD** with $u = 0.001$ (top right), **MBD** (bottom left), and **SD** (bottom right).

Model (C₂) *Central jump model*: For ϕ_1, \dots, ϕ_7 the first seven orthogonal polynomials on $[0, 1]$ as in Model (D₆) (maximum degree 6), we have $X = \mu + \sum_{j=1}^7 c_j \phi_j$, where $\mu(t) = 10t(1-t)$ and $(c_1, \dots, c_7)^\top$ is centered Gaussian with covariance matrix $\Sigma \in \mathbb{R}^{7 \times 7}$ with unit diagonal and 0.9 as off-diagonal terms, and $Y = \mu + \sum_{j=1}^5 d_j \phi_j + \sum_{j=6}^7 d_j \xi_j$, where $(d_1, \dots, d_7)^\top$ is Gaussian with mean $(0, \dots, 0, 1, 1)^\top \in \mathbb{R}^7$ and covariance matrix Σ as for X . Here, ξ_6, ξ_7 are the 11th and 12th B-spline basis functions of degree 3 with 21 equi-spaced knots on $[0, 1]$. The B-spline basis functions contribute to a significant jump in the center of the domain for Y , distinguishing these functions from X , see the middle panel of Figure 3.

Model (C₃) *Dimension difference model*: For X as in Model (C₂), $Y = \sum_{j=1}^5 d_j \phi_j$ with $(d_1, \dots, d_5)^\top$ Gaussian with mean the first eigenvector of $\Sigma_2 = \Sigma_{(5,5)}^{-1}/10$, where $\Sigma_{(5,5)} \in \mathbb{R}^{5 \times 5}$ is the first 5×5 sub-matrix of Σ from Model (C₂), and variance matrix Σ_2 . In this model, the dimensions of X and Y differ, and the functions differ in shape similarly to those in Model (D₆); see the right-hand panel of Figure 3.

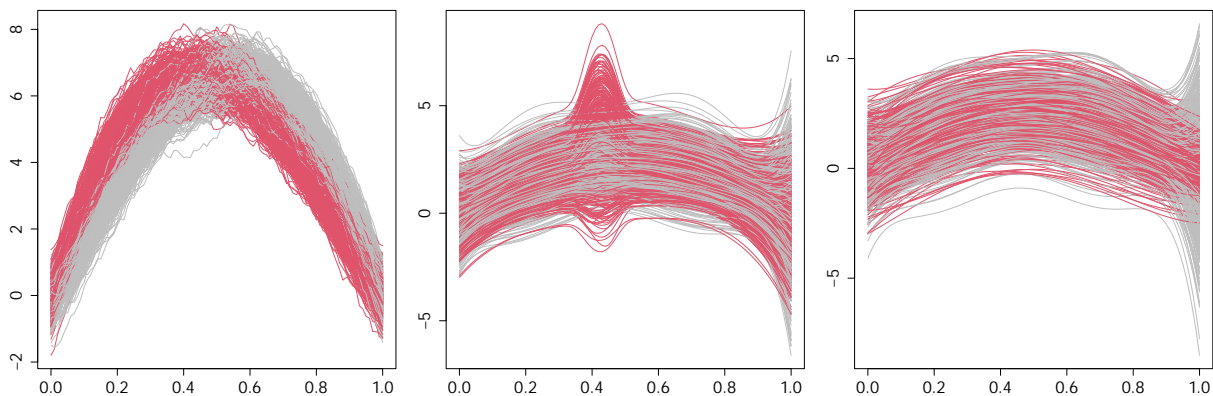


Figure 3: *Supervised classification*: A simulated dataset generated under Models (C₁)–(C₃) described in Section 4.2. The functions from class X (the first class) are shown in gray, while the functions from class Y (the second class) are in red.

For a function z and a depth D , its DD-transform (depth-depth transform) is defined as $(D(z; X), D(z; Y))^\top \in [0, 1]^2$, where $D(z; X)$ is the sample D -depth of z with respect to the sample from X , and analogously for Y . Two DD-classifiers are considered (Li et al., 2012):

- a max-depth classifier **max**, assigning a new datum z into the group where it attains higher D -depth, and
- the linear DD-classifier **DD**, with the rule based on the linear function (passing through the origin) that best separates the clusters $\{(D(X_i; X), D(X_i; Y))^\top\}_{i=1}^n$ and $\{(D(Y_i; X), D(Y_i; Y))^\top\}_{i=1}^n$.

For each classifier and each depth, we assess the out-sample empirical misclassification rate based on additional $n_{\text{test}} = 1000$ observations from each group (ties are handled by a fair coin toss, i.e., giving misclassification $1/2$). The means and standard deviations (in brackets) of the resulting misclassification rates in Models (C₁)–(C₃) over 100 independent runs of the simulation study are in Table 2.

Model	Classifier	RPD _{0.001}	RPD _{0.1}	RHD _{0.001}	RHD _{0.1}	FD	MBD	ID	SD
(C ₁)	max	0.013 (0.003)	0.014 (0.003)	0.068 (0.006)	0.060 (0.006)	0.068 (0.005)	0.057 (0.005)	0.068 (0.006)	0.022 (0.003)
	DD	0.014 (0.003)	0.014 (0.003)	0.069 (0.007)	0.061 (0.007)	0.069 (0.005)	0.058 (0.005)	0.068 (0.006)	0.023 (0.004)
(C ₂)	max	0.005 (0.002)	0.021 (0.005)	0.203 (0.038)	0.310 (0.050)	0.449 (0.044)	0.395 (0.050)	0.113 (0.039)	0.188 (0.043)
	DD	0.005 (0.002)	0.021 (0.005)	0.209 (0.037)	0.318 (0.075)	0.430 (0.036)	0.375 (0.043)	0.093 (0.029)	0.173 (0.041)
(C ₃)	max	0.078 (0.012)	0.086 (0.011)	0.246 (0.037)	0.427 (0.054)	0.493 (0.026)	0.433 (0.043)	0.212 (0.041)	0.290 (0.061)
	DD	0.029 (0.005)	0.060 (0.008)	0.247 (0.042)	0.428 (0.057)	0.483 (0.026)	0.423 (0.040)	0.154 (0.020)	0.273 (0.055)

Table 2: *Classification: Means and standard deviations (in brackets) of the empirical misclassification rates. The smallest misclassification rates are in bold.*

The results are clear-cut—**RPD** convincingly outperforms all its competitors in all scenarios. The results are striking, especially in Models (C₂) and (C₃) with shape differences. There, only **RPD** and (to a much smaller extent) **ID** and **RHD** are able to distinguish the two groups of data. It is important to note that, for the DD-plot based on **RPD**, a simple linear classifier is sufficient to effectively classify the two groups of complex functional data, such as those in Model (C₃). This is explained by the analysis of the resulting DD-plots for Model (C₃) in Figure 4, where the DD-transforms of the training data are displayed. Analogous diagnostic plots for Models (C₁) and (C₂) are in Appendix B.

From Table 2, we observe that **RPD** with regularization parameter $u = 0.1$ performs worse than **RPD** with $u = 0.001$. Therefore, also for classification, we generally recommend using a very small regularization parameter, such as $u = 0.001$, consistently with the outlier detection task.

4.3. Hypothesis testing

As a third application, we illustrate the practicality of the **RPD** through rank-based tests for assessing equality between distributions. Specifically, we construct the Kruskal–Wallis (KW) test statistic following the approach in Chenouri and Small (2012), using rankings derived from the **RPD**. When computing the KW statistic, tie corrections are applied as implemented in the `kruskal.test` function in R. For comparison, we also perform the same KW test procedures but replacing the **RPD** with other functional depths under consideration. All tests are conducted at the 5% significance level.

Since multi-sample extensions are straightforward, we restrict attention to two-sample observations $\{X_{k,i}\}_{i=1}^{n_k}$ for $k = 1, 2$. The functional observations are constructed by the expansion $X_{k,i} = \mu_k + \sum_{j=1}^{J_{\text{true}}} \gamma_{k,j}^{1/2} \xi_{k,i,j} \phi_{k,j}$ for $i = 1, \dots, n_k$ and $k = 1, 2$, with $J_{\text{true}} = 10$. For both groups, the scores $\xi_{k,i,j}$ are independently drawn from the standard normal distributions and the eigenvalues are determined by the eigengaps as $\gamma_{k,j} - \gamma_{k,j+1} = 2j^{-a_k}$ with decay rate $a_k \in (2, \infty)$, where $\gamma_{k,1} = 2 \sum_{j=1}^{\infty} j^{-a_k}$. The sample sizes are $n_1 = n_2 = n/2$ with total $n = 50$.

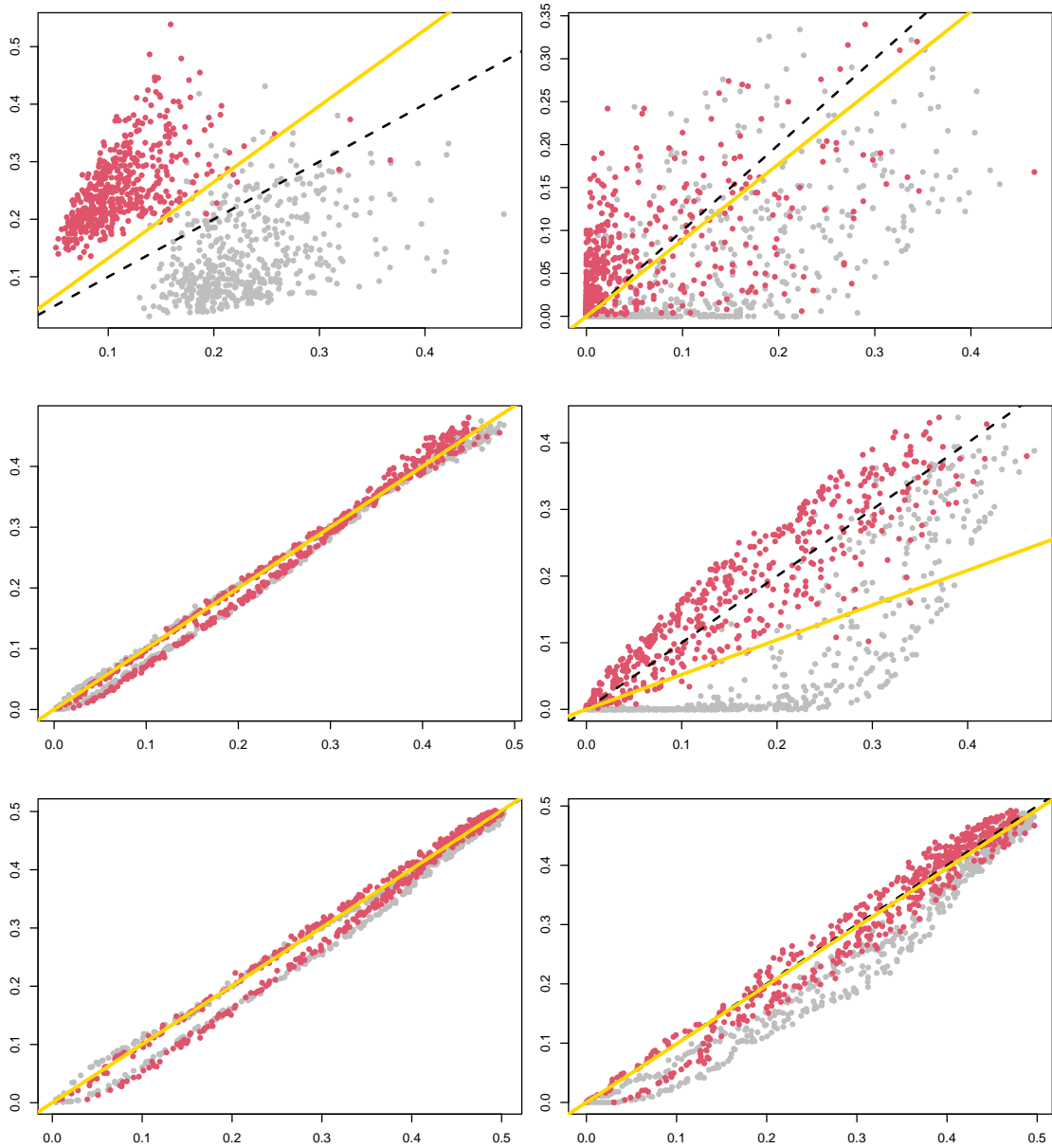


Figure 4: *Supervised classification: DD-plots of the training data in a single run of Model (C_3) (gray points for X_i , red points for Y_i) with (a) **RPD** (top left, $u = 0.001$), (b) **RHD** (top right, $u = 0.001$), (c) **FD** (middle left), (d) **ID** (middle right), (e) **MBD** (bottom left), and (f) **SD** (bottom right). In the plots, the dashed line represents the max-depth classifier and the orange line the linear DD-classifier best separating the two groups. The results are striking—while **RPD** with DD-classifier achieves almost perfect separation of the clouds, **FD**, **MBD**, and **SD** are unable to cope with the shape difference between the clusters. **RHD** and **ID** perform slightly better, but the overlap of the two DD-clouds is substantial.*

To investigate diverse types of group differences, we fix the parameters for the first group $\{X_{1,i}\}_{i=1}^{n_1}$ but only vary those for the second group $\{X_{2,i}\}_{i=1}^{n_2}$. The mean of the first group is set to be zero as $\mu_1(t) = 0$, $t \in [0, 1]$, while its eigengap decay rate is $a_1 = 5$. The eigenfunctions are the first $J_{\text{true}} = 10$ trigonometric functions, i.e., $\phi_{1,j} = \phi_{\text{tri},j}$ for $j = 1, \dots, J_{\text{true}}$, where $\{\phi_{\text{tri},j}\}_{j=1}^{\infty}$ is defined by

$$\phi_{\text{tri},1}(t) = 1, \quad \phi_{\text{tri},2m}(t) = \sqrt{2} \sin(2m\pi t), \quad \phi_{\text{tri},2m+1}(t) = \sqrt{2} \cos(2m\pi t), \quad t \in [0, 1], \quad m \in \mathbb{N}.$$

To create scenarios with different alternatives, we consider the following quantities: (i) $\mu_{\text{mag}}(t) = 3$ and (ii) $\mu_{\text{sin}}(t) = 1.2 \sin(2\pi t)$ for $t \in [0, 1]$, (iii) a decreasing sequence $\{\gamma_{\text{rough},j}\}_{j=1}^{\infty}$ defined by gap $\gamma_{\text{rough},j} - \gamma_{\text{rough},j+1} = 2j^{-a_{\text{rough}}}$ with decay rate $a_{\text{rough}} = 2.5$ where $\gamma_{\text{rough},1} = 2 \sum_{j=1}^{\infty} j^{-a_{\text{rough}}}$, and (iv) an orthonormal subset with high frequency $\{\phi_{\text{hfq},j}\}_{j=1}^{J_{\text{true}}}$ where $\phi_{\text{hfq},j} = \phi_{\text{tri},j+J_{\text{true}}}$ for $j = 1, \dots, J_{\text{true}}$. With parameter $c \in \{0, 0.2, 0.4, 0.6, 0.8, 1\}$ representing the degree of severity of alternatives, we consider the following four scenarios.

Model (T₁) *Magnitude difference in means:* $\mu_2 = c\mu_{\text{mag}}$ but $\gamma_{2,j} = \gamma_{1,j}$ and $\phi_{2,j} = \phi_{1,j}$.

Model (T₂) *Shape difference in means:* $\mu_2 = c\mu_{\text{sin}}$ but $\gamma_{2,j} = \gamma_{1,j}$ and $\phi_{2,j} = \phi_{1,j}$.

Model (T₃) *Difference in eigenvalues:* $a_2 = (1-c)a_1 + c a_{\text{rough}}$ but $\mu_2 = \mu_1$ and $\phi_{2,j} = \phi_{1,j}$.

Model (T₄) *Difference in eigenfunctions:* $\{\phi_{2,j}\}_{j=1}^{J_{\text{true}}}$ is the Gram-Schmidt orthonormalized set of $\{(1-c)\phi_{1,j} + c\phi_{\text{hfq},j}\}_{j=1}^{J_{\text{true}}}$ but $\mu_2 = \mu_1$ and $\gamma_{2,j} = \gamma_{1,j}$.

Note that in Models (T₁) and (T₂), the groups differ only in their means, whereas in (T₃) and (T₄), the difference lies solely in their second-order structure. One realization of these curves (with $c = 1$ for the second group) is depicted in Figure B.9 in Appendix B.

It is important to note that $c = 0$ renders the same null scenario in all Models (T₁)–(T₄), where the functional observations from both groups are equally distributed with mean zero, eigengap decay rate $a_1 = 5$, and eigenfunctions being the first $J_{\text{true}} = 10$ trigonometric functions.

The empirical sizes based on 1 000 independent replications of our study (which is common to all Models (T₁)–(T₄)) and the power of the KW tests are presented in Table 3 and Figure 5, respectively. Only the **RPD**-based tests achieve accurate size, whereas all other functional depths yield oversized tests. The **RHD**-based tests, among others, tend to impose overly stringent decisions. Since the remaining depth-based KW tests exhibit sizes that deviate substantially from the nominal level, we provide power results only for those with reasonable sizes, namely the **RPD**-, **FD**-, and **SD**-based KW tests, in Figure 5. Overall, the **RPD**-based KW tests consistently demonstrate strong power across scenarios, particularly in detecting differences driven by shape features.

RPD _{0.001}	RPD _{0.1}	RHD _{0.001}	RHD _{0.1}	FD	MBD	ID	SD
0.037	0.040	0.851	0.768	0.066	0.119	0.102	0.067

Table 3: *Hypothesis testing: Empirical sizes of the KW tests using depth-based rankings. The sizes within the range [0.03, 0.07] are written in bold.*

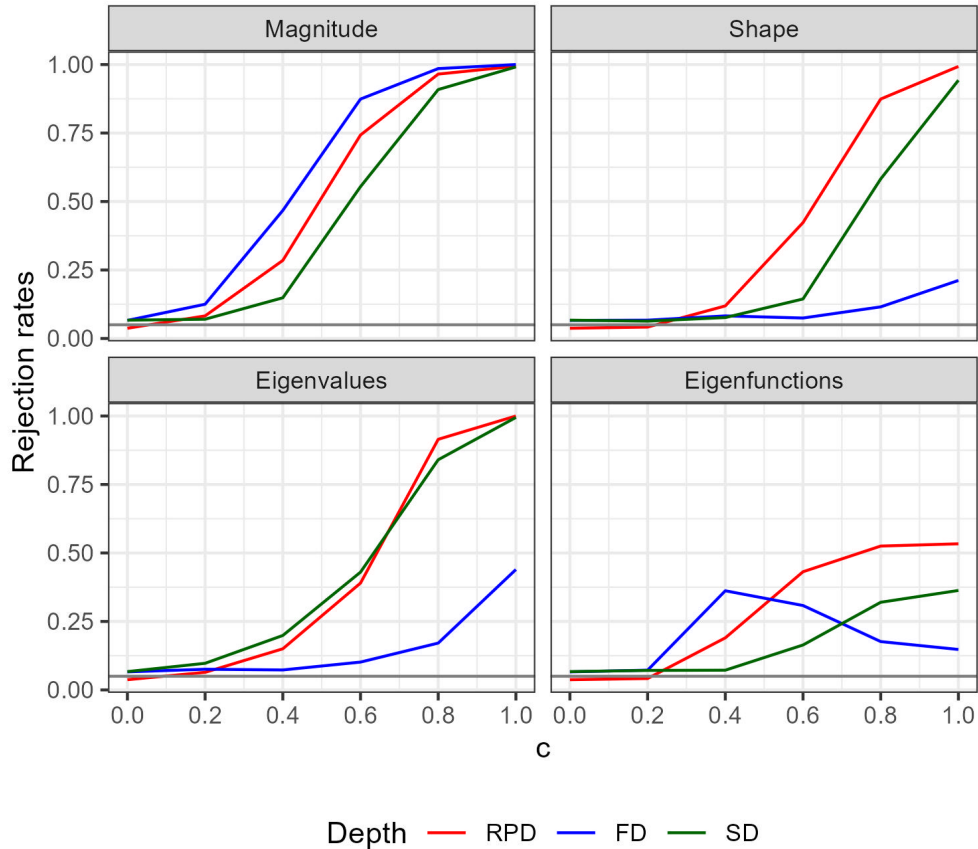


Figure 5: *Hypothesis testing: Empirical power of the KW tests using depth-based rankings. The results of the KW tests induced by depths other than **RPD**, **FD**, and **SD** are not reported, as they do not achieve correct nominal levels; see Table 3. Since the **RPD**-based tests with $u \in \{0.1, 0.001\}$ show similar results, only the results from the quantile level $u = 0.001$ are presented.*

4.4. Robust location estimation

In our final application, we consider robust location estimation in a functional setting. Motivated by contamination schemes commonly used in the functional data literature (see, for example, [Sinova et al. \(2018\)](#) and the references therein), we independently generate $n = 100$ random curves. Among these, $\lceil (1 - \varepsilon)n \rceil$ curves are sampled from the distribution of X , while the remaining $\lfloor \varepsilon n \rfloor$ curves are sampled from the distribution of Y , according to the following contamination models. Here, X represents the distribution of non-contaminated (clean) functional observations, while Y corresponds to the contaminating distribution. Throughout all models, X is a Gaussian process on $[0, 1]$ with mean function $\mu_X(t) = \sin(2\pi t)$ and covariance function $\Sigma(s, t) = 0.5 \exp(-|s - t|/10)$, $s, t \in [0, 1]$.

Model (\mathbf{L}_1) *Shift contamination model:* Y is a Gaussian process with mean function $\mu_Y(t) = \sin(2\pi t) + 1$ and covariance Σ .

Model (L₂) *Amplitude contamination model:* $Y \stackrel{d}{=} 2X$.

Model (L₃) *Phase contamination model:* Y is a Gaussian process with mean function $\mu_Y(t) = \sin(2\pi(t + 1/8))$ and covariance Σ .

Model (L₄) *Shape contamination model:* Y is a Gaussian process with mean function $\mu_Y(t) = \sin(2\pi t) + \sin(8\pi t)/6$ and covariance Σ .

Model (L₅) *Peak contamination model:* Y is a Gaussian process with mean function $\mu_Y(t) = \sin(2\pi t) + 2 \exp(-1000(t - 0.8)^2)$ and covariance Σ .

Illustrations of simulated datasets generated under these models are given in Figure B.10 in Appendix B.

To ensure a meaningful comparison of robustness properties across different depth notions, it is essential to identify a unique population median. Since that quantity is unambiguously defined only under symmetry assumptions, we restrict to symmetric non-contaminated reference distributions of X .

Our objective is to assess the robustness of depth-induced median functions under various contamination scenarios. For each depth, we define the location estimator $\hat{\mu}$ as the deepest curve in the generated sample. Its performance is evaluated using mean integrated squared error (MISE) which can be decomposed into variance term (IVAR) and squared bias term (ISB) as follows

$$\begin{aligned} \text{MISE}(\hat{\mu}) &= \mathbb{E} \|\hat{\mu} - \mu_X\|^2 = \mathbb{E} \int_0^1 (\hat{\mu}(t) - \mu_X(t))^2 dt = \int_0^1 \mathbb{E} (\hat{\mu}(t) - \mu_X(t))^2 dt \\ &= \int_0^1 \text{var}(\hat{\mu}(t) - \mu_X(t)) dt + \int_0^1 (\mathbb{E} \hat{\mu}(t) - \mu_X(t))^2 dt = \text{IVAR}(\hat{\mu}) + \text{ISB}(\hat{\mu}). \end{aligned} \tag{16}$$

For each Model (L₁)–(L₅), we estimate these quantities using the Monte Carlo method, where the experiment is repeated 500 times. In contrast to the previous tasks, where it was important for **RPD** to be sensitive to shape outliers, here the emphasis is on ensuring that the deepest functions are not overly influenced by such outliers. Based on the results in Section 2.2, we therefore consider higher regularization parameters $u \in \{0.1, 0.5\}$.

A complete summary of results for all models and depths is presented in Tables B.6 and B.7 in Appendix B. Here, we focus our discussion on Model (L₄). The results are summarized in Table 4. We first observe that the bias of the **RPD**-median is comparable to that of the other depth medians, and the results remain consistent across all depths. The differences in MISE are driven primarily by variance, with the **RPD**-median showing improved performance as u increases. This is in agreement with the results in Section 2.2, see Theorem 4 and the discussion there.

	ε	RPD _{0.1}	RPD _{0.5}	RHD _{0.1}	RHD _{0.5}	FD	MBD	ID	SD
ISB · 10 ³	0.000	0.015 (0.015)	0.021 (0.017)	0.011 (0.016)	0.026 (0.030)	0.006 (0.008)	0.007 (0.011)	0.017 (0.021)	0.005 (0.007)
	0.025	0.005 (0.007)	0.010 (0.009)	0.011 (0.013)	0.014 (0.016)	0.006 (0.014)	0.007 (0.011)	0.008 (0.010)	0.007 (0.008)
	0.050	0.049 (0.049)	0.022 (0.021)	0.019 (0.029)	0.014 (0.018)	0.007 (0.011)	0.007 (0.008)	0.013 (0.017)	0.010 (0.012)
	0.075	0.020 (0.026)	0.015 (0.018)	0.013 (0.024)	0.009 (0.008)	0.010 (0.012)	0.013 (0.014)	0.011 (0.019)	0.010 (0.011)
	0.100	0.018 (0.026)	0.020 (0.022)	0.023 (0.025)	0.025 (0.030)	0.022 (0.029)	0.020 (0.021)	0.010 (0.012)	0.020 (0.024)
IVAR · 10 ³	0.000	6.814 (0.503)	5.077 (0.445)	5.548 (0.581)	5.303 (0.916)	4.400 (0.931)	4.270 (0.629)	4.834 (0.392)	4.403 (0.474)
	0.025	7.026 (0.458)	5.079 (0.446)	5.279 (0.617)	5.564 (1.025)	4.463 (0.852)	4.313 (0.678)	4.978 (0.438)	4.660 (0.522)
	0.050	7.555 (0.361)	4.992 (0.445)	5.239 (0.512)	5.583 (0.911)	4.406 (0.750)	4.307 (0.612)	5.049 (0.417)	4.542 (0.466)
	0.075	7.692 (0.298)	5.590 (0.455)	5.481 (0.666)	5.581 (0.845)	4.627 (0.707)	4.538 (0.470)	5.123 (0.364)	4.689 (0.456)
	0.100	7.169 (0.409)	5.112 (0.418)	5.422 (0.575)	5.574 (0.886)	4.493 (0.842)	4.417 (0.653)	5.071 (0.359)	4.684 (0.515)
MISE · 10 ³	0.000	6.884 (0.512)	5.139 (0.443)	5.604 (0.584)	5.372 (0.927)	4.442 (0.938)	4.312 (0.634)	4.890 (0.406)	4.444 (0.479)
	0.025	7.088 (0.463)	5.130 (0.449)	5.333 (0.623)	5.623 (1.034)	4.505 (0.857)	4.354 (0.683)	5.026 (0.443)	4.705 (0.527)
	0.050	7.665 (0.371)	5.054 (0.450)	5.301 (0.532)	5.643 (0.928)	4.449 (0.758)	4.349 (0.620)	5.103 (0.428)	4.589 (0.473)
	0.075	7.774 (0.310)	5.651 (0.458)	5.539 (0.683)	5.635 (0.850)	4.675 (0.714)	4.588 (0.474)	5.175 (0.369)	4.737 (0.462)
	0.100	7.244 (0.424)	5.173 (0.428)	5.489 (0.580)	5.644 (0.902)	4.552 (0.865)	4.473 (0.667)	5.123 (0.364)	4.741 (0.528)

Table 4: *Robust location estimation: Comparison of performance measures for Model (L₄). The table reports ISB · 10³, IVAR · 10³, and MISE · 10³, as defined in (16), for various contamination levels ε . For each experimental setting, the deepest function is identified and the corresponding quantities are evaluated. Reported values are Monte Carlo averages with standard deviations in parentheses, based on 500 simulations.*

Taken together with the previous findings, these results suggest that the classical depth functions tend to overlook shape-related features of the data. Even so, the **RPD**-median continues to yield reasonable estimates by incorporating centrality as well as various types of outlyingness. Overall, we recommend selecting the quantile level u based on the underlying data structure. When outlyingness is of primary interest, smaller values such as $u = 0.001$ are preferable (Sections 4.1–4.3). In cases of simple functional models with low intrinsic complexity, larger quantile levels (including $u = 0.5$) may also be more appropriate, as observed in the present study.

To conclude, we consider one final model, which is a modification of Model (L₁) where the location shift is increased from 1 to 1000.

Model (L₆) *Large shift contamination model:* Y is a Gaussian process with mean function $\mu_Y(t) = \sin(2\pi t) + 1000$ and covariance Σ .

The resulting MISE values are reported in Table 5. Such a large shift substantially alters the variance structure of the dataset. Note that **RHD** estimates the variance structure using the classical sample covariance operator, which is not robust. In contrast, **RPD** employs the robust MAD for variance estimation. As can be seen, unlike the results for Model (L₁), the MISE under **RHD** is markedly higher in Model (L₆). This highlights the advantage of **RPD** over **RHD** in terms of the robustness of the induced median.

	ε	RPD _{0.1}	RPD _{0.5}	RHD _{0.1}	RHD _{0.5}	FD	MBD	ID	SD
MISE · 10 ³	0.000	7.057 (0.429)	5.158 (0.465)	5.206 (0.531)	5.427 (0.876)	4.338 (0.844)	4.275 (0.612)	4.898 (0.418)	4.417 (0.510)
	0.025	7.048 (0.377)	5.058 (0.492)	13.144 (4.326)	13.581 (4.503)	4.391 (0.743)	4.273 (0.657)	4.980 (0.438)	4.484 (0.519)
	0.050	7.574 (0.376)	5.544 (0.427)	13.920 (4.143)	13.752 (4.099)	4.797 (0.762)	4.670 (0.566)	5.455 (0.544)	4.687 (0.400)
	0.075	8.068 (0.487)	5.797 (0.536)	13.613 (4.187)	13.723 (4.237)	5.136 (0.956)	5.096 (0.757)	6.047 (0.491)	5.174 (0.668)
	0.100	9.635 (0.401)	6.663 (0.583)	13.925 (4.628)	14.015 (4.672)	5.714 (0.883)	5.633 (0.750)	6.723 (0.403)	5.909 (0.615)

Table 5: *Robust location estimation: Comparison of performance for Model (L₆). The table reports MISE · 10³, as defined in (16), for various contamination levels ε . For each experimental setting, the deepest function is identified and the corresponding quantities are evaluated. Reported values are Monte Carlo averages with standard deviations in parentheses, based on 500 simulations.*

References

- Arribas-Gil, A., Romo, J., 2014. Shape outlier detection and visualization for functional data: the outliergram. *Biostatistics* 15, 603–619.
- Boente, G., Salibián Barrera, M., Tyler, D.E., 2014. A characterization of elliptical distributions and some optimality properties of principal components for functional data. *J. Multivariate Anal.* 131, 254–264.
- Boćinec, F., Nagy, S., Yeon, H., 2026. Projection depth for functional data: Theoretical properties. Manuscript under review.
- Briend, S., Lugosi, G., Oliveira, R.I., 2025. On the quality of randomized approximations of Tukey’s depth. *SIAM J. Math. Data Sci.* 7, 1441–1464.
- Chakraborty, A., Chaudhuri, P., 2014a. The deepest point for distributions in infinite dimensional spaces. *Stat. Methodol.* 20, 27–39.
- Chakraborty, A., Chaudhuri, P., 2014b. On data depth in infinite dimensional spaces. *Ann. Inst. Statist. Math.* 66, 303–324.
- Chaudhuri, P., 1996. On a geometric notion of quantiles for multivariate data. *J. Amer. Statist. Assoc.* 91, 862–872.
- Chenouri, S., Small, C.G., 2012. A nonparametric multivariate multisample test based on data depth. *Electron. J. Statist.* 6, 760–782.
- Cuevas, A., Febrero, M., Fraiman, R., 2007. Robust estimation and classification for functional data via projection-based depth notions. *Comput. Statist.* 22, 481–496.
- Donoho, D.L., 1982. Breakdown properties of multivariate location estimators. Qualifying paper, Harvard University.
- Dudley, R.M., 2002. Real analysis and probability. volume 74 of *Cambridge Studies in Advanced Mathematics*. Cambridge University Press, Cambridge. Revised reprint of the 1989 original.
- Dyckerhoff, R., 2004. Data depths satisfying the projection property. *Allg. Stat. Arch.* 88, 163–190.
- Eddelbuettel, D., Francois, R., Bates, D., Ni, B., Sanderson, C., 2024. RcppArmadillo: ‘Rcpp’ integration for the ‘Armadillo’ templated linear algebra library. URL: <https://CRAN.R-project.org/package=RcppArmadillo>. R package version 14.2.2-1.
- Elmore, R.T., Hettmansperger, T.P., Xuan, F., 2006. Spherical data depth and a multivariate median, in: Data depth: robust multivariate analysis, computational geometry and applications. Amer. Math. Soc., Providence, RI. volume 72 of *DIMACS Ser. Discrete Math. Theoret. Comput. Sci.*, pp. 87–101.
- Fraiman, R., Muniz, G., 2001. Trimmed means for functional data. *Test* 10, 419–440.

- Helander, S., Van Bever, G., Rantala, S., Ilmonen, P., 2020. Pareto depth for functional data. *Statistics* 54, 182–204.
- Hlubinka, D., Gijbels, I., Omelka, M., Nagy, S., 2015. Integrated data depth for smooth functions and its application in supervised classification. *Comput. Statist.* 30, 1011–1031.
- Hsing, T., Eubank, R., 2015. Theoretical foundations of functional data analysis, with an introduction to linear operators. *Wiley Series in Probability and Statistics*, John Wiley & Sons, Ltd., Chichester.
- Huber, P.J., 1985. Projection pursuit. *Ann. Statist.* 13, 435–525.
- Huber, P.J., Ronchetti, E.M., 2009. Robust statistics. *Wiley Series in Probability and Statistics*, second ed., John Wiley & Sons, Inc., Hoboken, NJ.
- Hubert, M., Rousseeuw, P., Segaert, P., 2017. Multivariate and functional classification using depth and distance. *Adv. Data Anal. Classif.* 11, 445–466.
- Jiménez-Varón, C.F., Harrou, F., Sun, Y., 2024. Pointwise data depth for univariate and multivariate functional outlier detection. *Environmetrics* 35, Paper No. e2851, 19.
- Kong, L., Zuo, Y., 2010. Smooth depth contours characterize the underlying distribution. *J. Multivariate Anal.* 101, 2222–2226.
- Kuo, H.H., 1975. Gaussian measures in Banach spaces. volume Vol. 463 of *Lecture Notes in Mathematics*. Springer-Verlag, Berlin-New York.
- Li, J., Cuesta-Albertos, J.A., Liu, R.Y., 2012. *DD*-classifier: nonparametric classification procedure based on *DD*-plot. *J. Amer. Statist. Assoc.* 107, 737–753.
- Liu, R.Y., 1990. On a notion of data depth based on random simplices. *Ann. Statist.* 18, 405–414.
- Liu, X., Zuo, Y., 2014. Computing projection depth and its associated estimators. *Stat. Comput.* 24, 51–63.
- López-Pintado, S., Romo, J., 2009. On the concept of depth for functional data. *J. Amer. Statist. Assoc.* 104, 718–734.
- Mendroš, E., Nagy, S., 2025. The spherical depth for functional data, in: *New trends in functional statistics and related fields*. Springer, Cham. *Contrib. Stat.*, pp. 401–408.
- Mosler, K., 2002. Multivariate dispersion, central regions and depth: The lift zonoid approach. volume 165 of *Lecture Notes in Statistics*. Springer-Verlag, Berlin.
- Mosler, K., 2013. Depth statistics, in: Becker, C., Fried, R., Kuhnt, S. (Eds.), *Robustness and complex data structures*. Springer, Heidelberg, pp. 17–34.
- Nagy, S., Gijbels, I., Hlubinka, D., 2017. Depth-based recognition of shape outlying functions. *J. Comput. Graph. Statist.* 26, 883–893.
- Nagy, S., Gijbels, I., Omelka, M., Hlubinka, D., 2016. Integrated depth for functional data: Statistical properties and consistency. *ESAIM Probab. Stat.* 20, 95–130.
- Narisetty, N.N., Nair, V.N., 2016. Extremal depth for functional data and applications. *J. Amer. Statist. Assoc.* 111, 1705–1714.
- Ojo, O.T., Fernández Anta, A., Lillo, R.E., Sguera, C., 2022. Detecting and classifying outliers in big functional data. *Adv. Data Anal. Classif.* 16, 725–760.
- Ramsay, K., Chenouri, S., 2024. Robust nonparametric hypothesis tests for differences in the covariance structure of functional data. *Canad. J. Statist.* 52, 43–78.
- Serfling, R., 1980. Approximation theorems of mathematical statistics. John Wiley & Sons Inc., New York. *Wiley Series in Probability and Mathematical Statistics*.
- Shao, W., Zuo, Y., Luo, J., 2022. Employing the MCMC technique to compute the projection

- depth in high dimensions. *J. Comput. Appl. Math.* 411, Paper No. 114278, 16.
- Sinova, B., González-Rodríguez, G., Van Aelst, S., 2018. M-estimators of location for functional data. *Bernoulli* 24, 2328–2357.
- Stahel, W.A., 1981. Robuste Schätzungen: Infinitesimale Optimalität und Schätzungen von Kovarianzmatrizen. Ph.D. thesis, ETH Zürich.
- Sun, Y., Genton, M.G., 2011. Functional boxplots. *J. Comput. Graph. Statist.* 20, 316–334.
- Tukey, J.W., 1975. Mathematics and the picturing of data, in: *Proceedings of the International Congress of Mathematicians (Vancouver, B. C., 1974)*, Vol. 2, *Canad. Math. Congress*, Montreal, Que. pp. 523–531.
- Yeon, H., Dai, X., López-Pintado, S., 2025. Regularized halfspace depth for functional data. *J. R. Stat. Soc. Ser. B Stat. Methodol.* 87, 1553–1575.
- Zuo, Y., 2003. Projection-based depth functions and associated medians. *Ann. Statist.* 31, 1460–1490.

Appendix A. Proofs of theoretical results

Proof of Lemma 1. Note that it suffices to prove that $\nu(\{v \in \mathbb{S} : \text{MAD}[\langle X, v \rangle] = 0\}) = 0$. Assume, for a contradiction, that this is not true. First note that for any $v \in \mathbb{S}$ fixed, we have that $\text{MAD}[\langle X, v \rangle] = 0$ if and only if $\langle X, v \rangle = \text{med}[\langle X, v \rangle]$ with probability at least $1/2$. Consequently, if we denote

$$B = \{v \in \mathbb{S} : P_X(\{y \in \mathbb{H} : \langle y, v \rangle = \text{med}[\langle X, v \rangle]\}) \geq 1/2\},$$

then $\nu(B) > 0$. Consider the set

$$E = \{(y, v) \in \mathbb{H} \times B : \langle y, v \rangle = \text{med}[\langle X, v \rangle]\}.$$

By the Fubini-Tonelli theorem (Dudley, 2002, Theorem 4.4.5),

$$\begin{aligned} \int_{\mathbb{H}} \nu(\{v \in B : \langle y, v \rangle = \text{med}[\langle X, v \rangle]\}) dP_X(y) &= \int_{\mathbb{H}} \int_B \mathbf{1}_E(y, v) d\nu(v) dP_X(y) \\ &= \int_B \int_{\mathbb{H}} \mathbf{1}_E(y, v) dP_X(y) d\nu(v) = \int_B P_X(\{y \in \mathbb{H} : \langle y, v \rangle = \text{med}[\langle X, v \rangle]\}) d\nu(v) \\ &\geq \frac{1}{2} \int_B d\nu(v) = \nu(B)/2 > 0, \end{aligned}$$

where $\mathbf{1}_E(y, v) = 1$ if $(y, v) \in E$ and 0 elsewhere, and the inequality above follows from the definition of B . As a consequence, there must exist $x \in \mathbb{H}$ such that

$$\nu(\{v \in B : \langle x, v \rangle = \text{med}[\langle X, v \rangle]\}) > 0, \tag{A.1}$$

that is, the set of normal vectors $v \in \mathbb{S}$ of hyperplanes of probability at least $1/2$ containing this particular point x has positive ν -measure. We will show that x is indeed the desired atom with probability at least $1/2$.

Let $X' \stackrel{d}{=} X - x$ and

$$\begin{aligned} B' &= \{v \in B : P_X(\{y \in \mathbb{H} : \langle y, v \rangle = \langle x, v \rangle\}) \geq 1/2\} \\ &= \{v \in B : P_{X'}(\{y \in \mathbb{H} : \langle y, v \rangle = 0\}) \geq 1/2\}. \end{aligned}$$

By (A.1) we know that $\nu(B') > 0$. We will use the Fubini-Tonelli theorem again for the set $G = \{(y, v) \in \mathbb{H} \times B' : \langle y, v \rangle = 0\}$. We obtain

$$\begin{aligned} \int_{\mathbb{H}} \nu(\{v \in B' : \langle y, v \rangle = 0\}) dP_{X'}(y) &= \int_{\mathbb{H}} \int_{B'} \mathbf{1}_G(y, v) d\nu(v) dP_{X'}(y) \\ &= \int_{B'} \int_{\mathbb{H}} \mathbf{1}_G(y, v) dP_{X'}(y) d\nu(v) = \int_{B'} P_{X'}(\{y \in \mathbb{H} : \langle y, v \rangle = 0\}) d\nu(v) \\ &\geq \frac{1}{2} \int_{B'} d\nu(v) = \nu(B')/2. \end{aligned} \tag{A.2}$$

Note that $\nu(\{v \in B' : \langle y, v \rangle = 0\})$ can be non-zero only for $y = 0$, because ν is smooth. As a consequence,

$$\int_{\mathbb{H}} \nu(\{v \in B' : \langle y, v \rangle = 0\}) dP_{X'}(y) = \nu(B')P_{X'}(\{0\}),$$

which together with (A.2) implies $P_{X'}(\{0\}) \geq 1/2$. This proves that X' has atom $0 \in \mathbb{H}$ with probability at least $1/2$, which is a contradiction. \square

Proof of Lemma 2. By [B, Lemma 12], it holds that

$$\sup_{v \in \mathbb{S}} \left| \widehat{\text{MAD}}[\{\langle X_i, v \rangle\}_{i=1}^n] - \text{MAD}[\langle X, v \rangle] \right| \xrightarrow[n \rightarrow \infty]{\text{a.s.}} 0.$$

This means that $\widehat{\text{MAD}}[\{\langle X_i, V(\omega) \rangle\}_{i=1}^n]$ converges to $\text{MAD}[\langle X, V(\omega) \rangle]$ for every $\omega \in \Omega$. Consequently $\widehat{\text{MAD}}[\{\langle X_i, V \rangle\}_{i=1}^n]$ converges to $\text{MAD}[\langle X, V \rangle]$ in distribution. The claim follows from Serfling (1980, Section 2.3) using the continuity assumption. \square

Proof of Theorem 3. The proof follows directly from the argument of [B, Theorem 7]. Specifically, using the 1-Lipschitz continuity of the function $t \mapsto 1/(1+t)$, $t \geq 0$, we can write

$$\begin{aligned} & \sup_{x \in \mathcal{F}} \left| D_{(u)}(x; \widehat{P}_n) - D_{(u)}(x; P_X) \right| \leq \sup_{x \in \mathcal{F}} \left| \sup_{v \in \widehat{\mathcal{V}}_n(u)} O_v(x; \widehat{P}_n) - \sup_{v \in \mathcal{V}(u)} O_v(x; P_X) \right| \\ & \leq \sup_{x \in \mathcal{F}} \left| \sup_{v \in \widehat{\mathcal{V}}_n(u)} O_v(x; \widehat{P}_n) - \sup_{v \in \widehat{\mathcal{V}}_n(u)} O_v(x; P_X) \right| + \sup_{x \in \mathcal{F}} \left| \sup_{v \in \widehat{\mathcal{V}}_n(u)} O_v(x; P_X) - \sup_{v \in \mathcal{V}(u)} O_v(x; P_X) \right|. \end{aligned}$$

The first term converges to zero a.s. by the same arguments as in [B, Theorem 7]. Consequently, the only remaining step is to show that

$$\left| \sup_{v \in \widehat{\mathcal{V}}_n(u)} O_v(x; P_X) - \sup_{v \in \mathcal{V}(u)} O_v(x; P_X) \right| \xrightarrow[n \rightarrow \infty]{\text{a.s.}} 0.$$

This convergence follows immediately from Lemma 2 together with (9). \square

Proof of Theorem 4. Fix $\varepsilon \in (0, 1/2)$. Because condition (13) holds, choose $\gamma > 0$ such that $\nu(A) \geq 1 - \varepsilon$, where

$$A = \left\{ v \in \mathbb{S} : \omega_v(\gamma) \leq \frac{1/2 - \varepsilon}{1 - \varepsilon} \right\}.$$

For any $Q \in \mathcal{P}(\mathbb{H})$, $X' \sim P_{(Q, \varepsilon)}$, $v \in A$ and $a \in \mathbb{R}$, we have

$$\begin{aligned} \mathbb{P}(\langle X', v \rangle \in (a - \gamma/2, a + \gamma/2)) & \leq (1 - \varepsilon)\mathbb{P}(\langle X, v \rangle \in (a - \gamma/2, a + \gamma/2)) + \varepsilon \\ & \leq (1 - \varepsilon)\omega_v(\gamma) + \varepsilon \leq \frac{1}{2} - \varepsilon + \varepsilon = \frac{1}{2}. \end{aligned}$$

Hence, for $v \in A$ and any $Q \in \mathcal{P}(\mathbb{H})$, it follows that $\text{MAD}[\langle X', v \rangle] \geq \gamma$. Since $\nu(A) \geq 1 - u$, we obtain

$$\inf_Q \beta_{(Q, \varepsilon)}(u) \geq \gamma. \quad (\text{A.3})$$

Next, as in [B, Theorem 10], for $X' \sim P_{(Q, \varepsilon)}$ we can bound

$$\text{med}[\langle X', v \rangle] \leq \text{med}[\|X'\|] \leq q, \quad (\text{A.4})$$

where $q > 0$ denotes the $(1/2 + \varepsilon)$ -quantile of $\|X\|$. The upper bound (A.4) follows from the fact that the ε -contaminated distribution $P_{(Q, \varepsilon)}$ differs from P_X by at most an ε -fraction of its mass. Therefore, the median of $\|X'\|$ under $P_{(Q, \varepsilon)}$ cannot exceed the $(1/2 + \varepsilon)$ -quantile of $\|X\|$ under P_X . Similarly

$$\text{MAD}[\langle X', v \rangle] \leq 2 \text{med}[\|X'\|] \leq 2q. \quad (\text{A.5})$$

Since $\theta(P_{(Q, \varepsilon)})$ maximizes $D_{(u)}(\cdot; P_{(Q, \varepsilon)})$ over $\text{cl}(\text{span}(\mathcal{V}_{(u)}(Q, \varepsilon)))$, its outlyingness cannot exceed that of $0 \in \text{cl}(\text{span}(\mathcal{V}_{(u)}(Q, \varepsilon)))$. Therefore, by (A.4) and (A.5)

$$\begin{aligned} \sup_{v \in \mathcal{V}_{(u)}(Q, \varepsilon)} O_v(0; P_{(Q, \varepsilon)}) &\geq \sup_{v \in \mathcal{V}_{(u)}(Q, \varepsilon)} O_v(\theta(P_{(Q, \varepsilon)}); P_{(Q, \varepsilon)}) \\ &\geq \frac{\sup_{v \in \mathcal{V}_{(u)}(Q, \varepsilon)} |\langle \theta(P_{(Q, \varepsilon)}), v \rangle| - \sup_{v \in \mathbb{S}} |\text{med}[\langle X', v \rangle]|}{\sup_{v \in \mathbb{S}} \text{MAD}[\langle X', v \rangle]} \\ &\geq \frac{\sup_{v \in \mathcal{V}_{(u)}(Q, \varepsilon)} |\langle \theta(P_{(Q, \varepsilon)}), v \rangle| - q}{2q}. \end{aligned} \quad (\text{A.6})$$

On the other hand, by (A.3) and (A.4)

$$\sup_{v \in \mathcal{V}_{(u)}(Q, \varepsilon)} O_v(0; P_{(Q, \varepsilon)}) \leq \frac{\sup_{v \in \mathbb{S}} |\text{med}[\langle X', v \rangle]|}{\beta_{(Q, \varepsilon)}(u)} \leq q/\gamma. \quad (\text{A.7})$$

Combining the inequalities (A.6) and (A.7) yields

$$\sup_{v \in \mathcal{V}_{(u)}(Q, \varepsilon)} |\langle \theta(P_{(Q, \varepsilon)}), v \rangle| \leq \frac{2q^2}{\gamma} + q < \infty,$$

proving that the RPD median cannot break down under the considered contamination. \square

Proof of Theorem 5. First, because $\beta(u)$ is uniquely defined, $\beta^{(L)}(u)$ consistently estimates $\beta(u)$ in the sense that $\beta^{(L)}(u) \rightarrow \beta(u)$ a.s. as $L \rightarrow \infty$ (Serfling, 1980, Section 2.3). Next, note that

$$\begin{aligned} \left| D_{(u)}^{(M)}(x; P_X) - D_{(u)}(x; P_X) \right| &= \left| D_{(u)}^{(M)}(x; P_X) - D_{\beta(u)}(x; P_X) \right| \\ &\leq \left| D_{(u)}^{(M)}(x; P_X) - D_{\beta^{(L)}(u)}(x; P_X) \right| + \left| D_{\beta^{(L)}(u)}(x; P_X) - D_{(u)}(x; P_X) \right|. \end{aligned}$$

The second summand equals

$$|\Gamma_x(\beta^{(L)}(u)) - \Gamma_x(\beta(u))|,$$

which converges to 0 a.s. as $L \rightarrow \infty$ since $\Gamma_x(\cdot)$ is continuous at $\beta(u)$ and by the consistency of $\beta^{(L)}(u)$. The rest of the proof follows directly from the arguments of [Dyckerhoff \(2004, Proposition 11\)](#). The only difference is that we are taking infimum over $\mathcal{V}_{\beta^{(L)}(u)}$, but since ν does not vanish on \mathbb{S} , it also does not vanish on its closed non-empty subset $\mathcal{V}_{\beta^{(L)}(u)}$. \square

Appendix B. Simulation study: Supplementary results

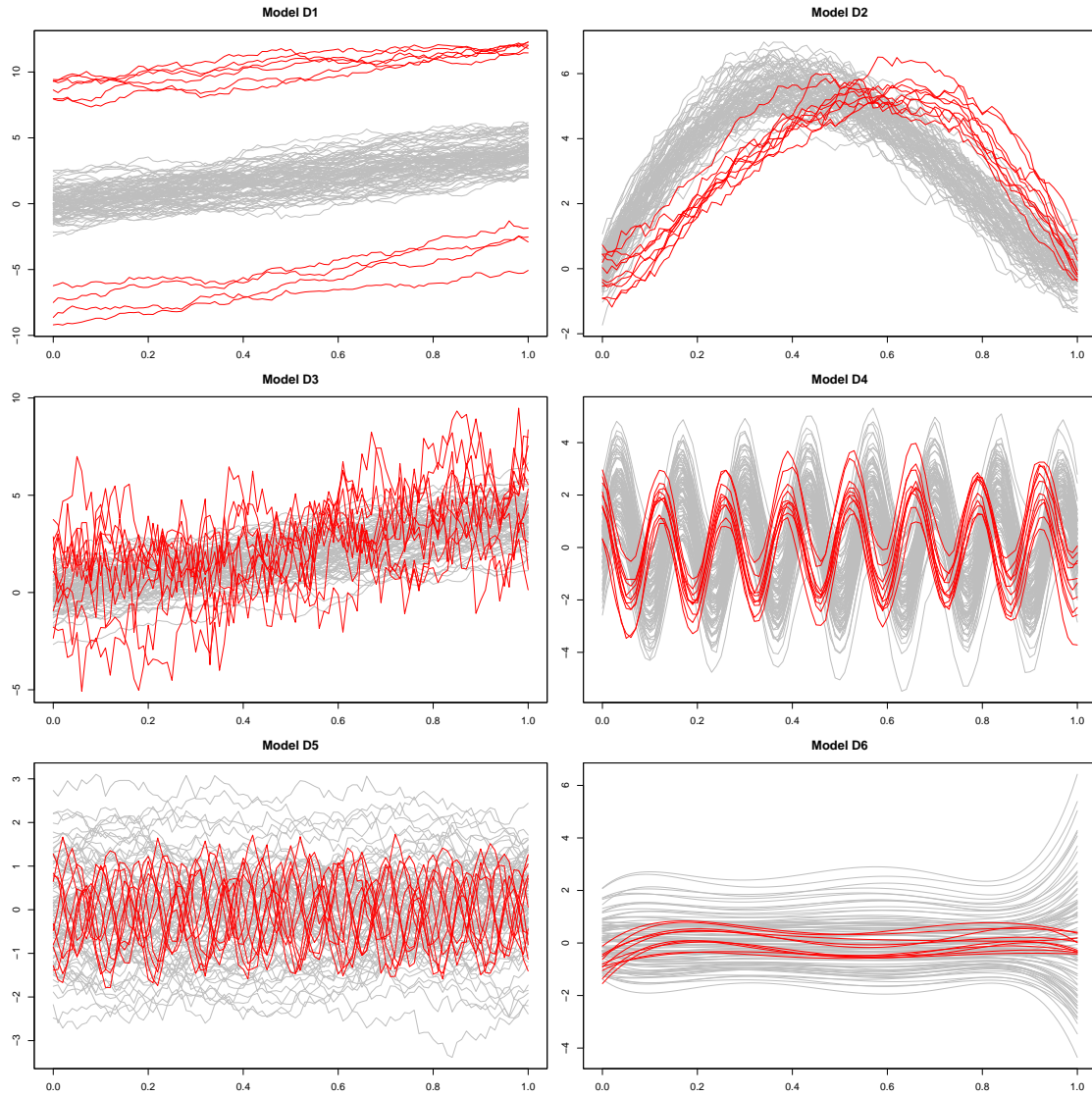


Figure B.6: *Outlier detection: Simulated datasets generated under the contamination Models (D_1)–(D_6) described in Section 4.1. Each panel contains 100 functions, of which 10 are contaminated. The non-contaminated functions are shown in gray, while the contaminating functions are highlighted in red.*

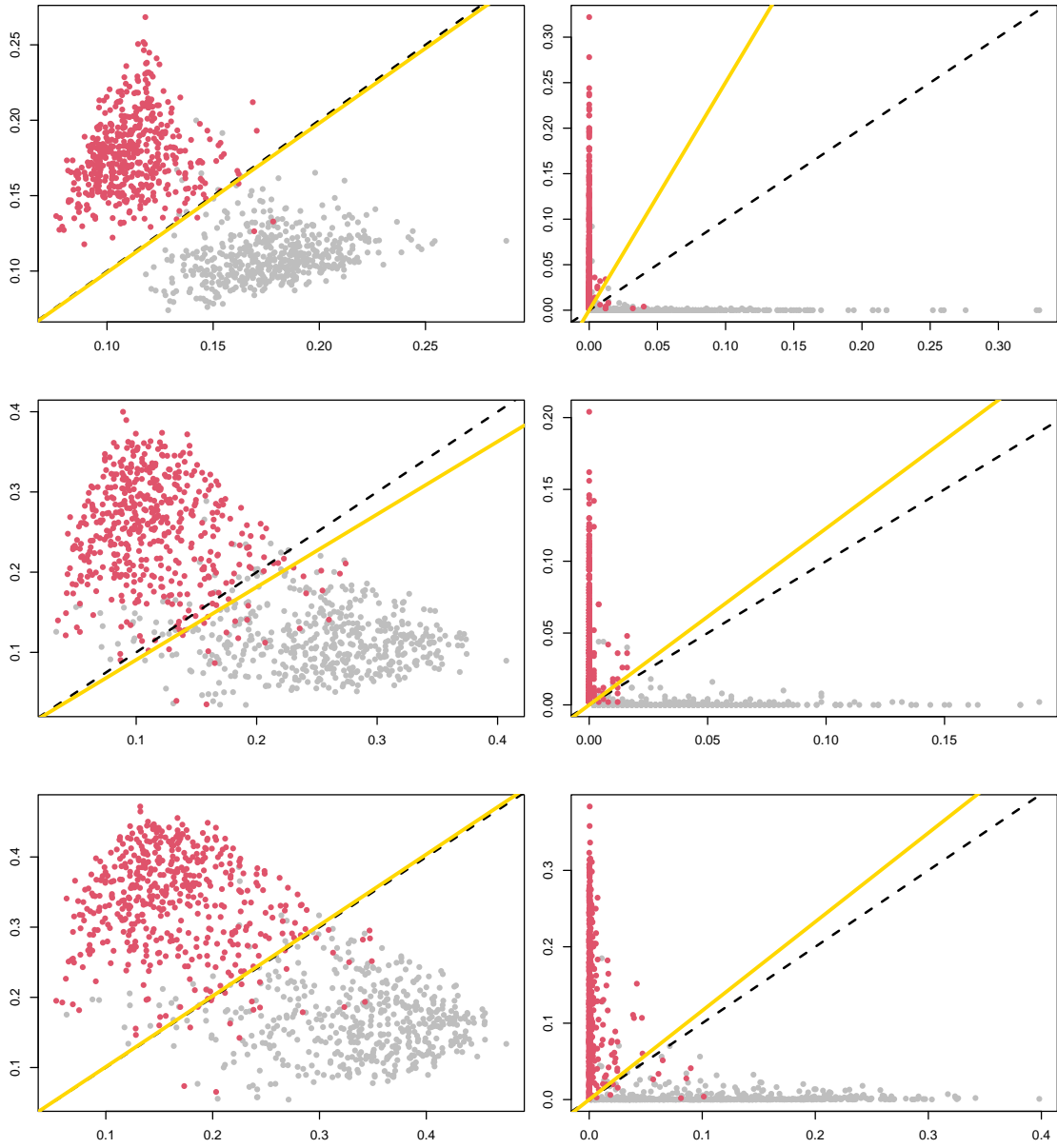


Figure B.7: *Supervised classification: DD-plots of the training data in a single run of Model (C_1) (gray points for X_i , red points for Y_i) with (a) **RPD** (top left, $u = 0.001$), (b) **RHD** (top right, $u = 0.001$), (c) **FD** (middle left), (d) **ID** (middle right), (e) **MBD** (bottom left), and (f) **SD** (bottom right). In the plots, the dashed line represents the max-depth classifier and the orange line the linear DD-classifier best separating the two groups.*

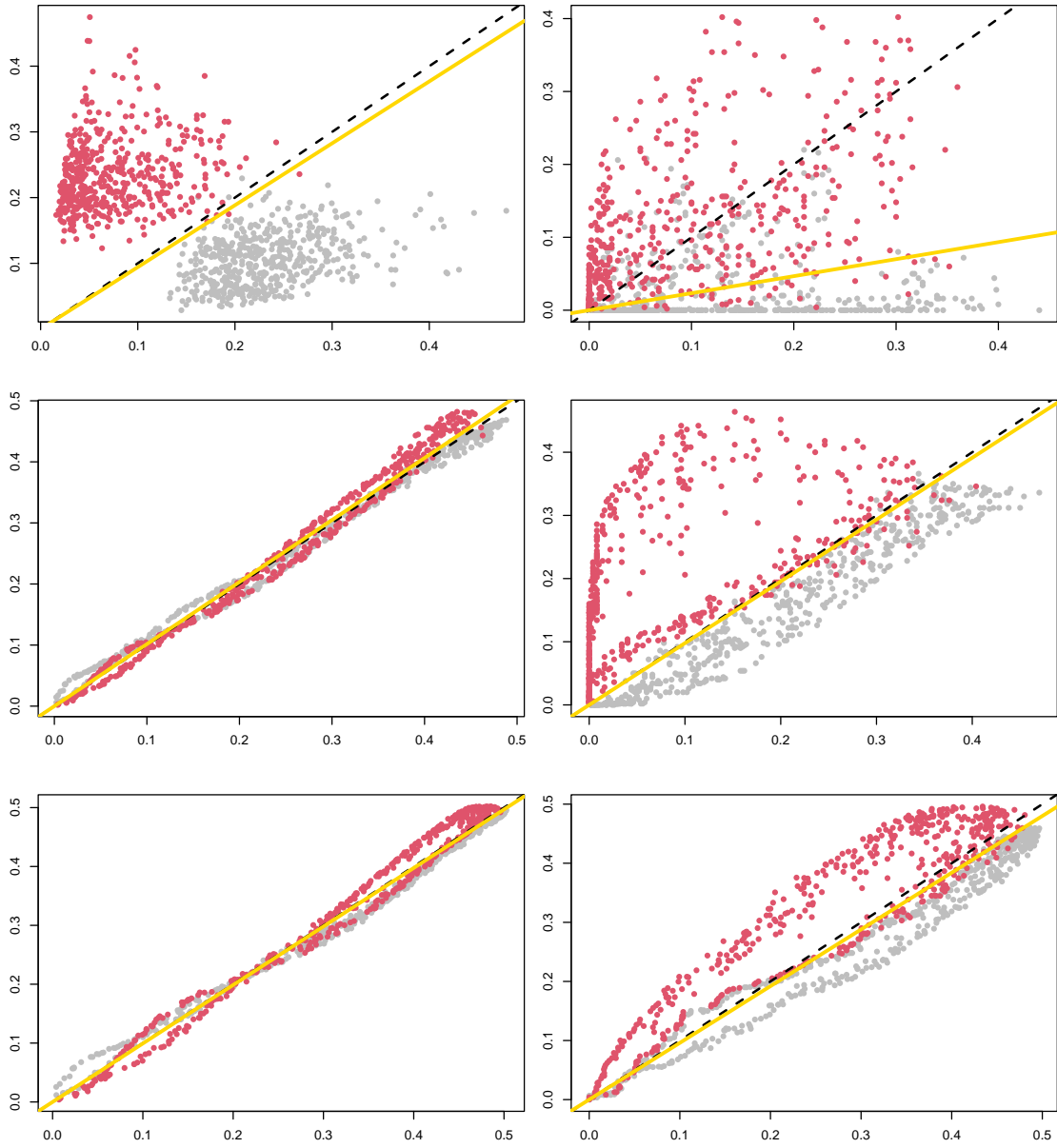


Figure B.8: *Supervised classification: DD-plots of the training data in a single run of Model (C_2) (gray points for X_i , red points for Y_i) with (a) **RPD** (top left, $u = 0.001$), (b) **RHD** (top right, $u = 0.001$), (c) **FD** (middle left), (d) **ID** (middle right), (e) **MBD** (bottom left), and (f) **SD** (bottom right). In the plots, the dashed line represents the max-depth classifier and the orange line the linear DD-classifier best separating the two groups.*

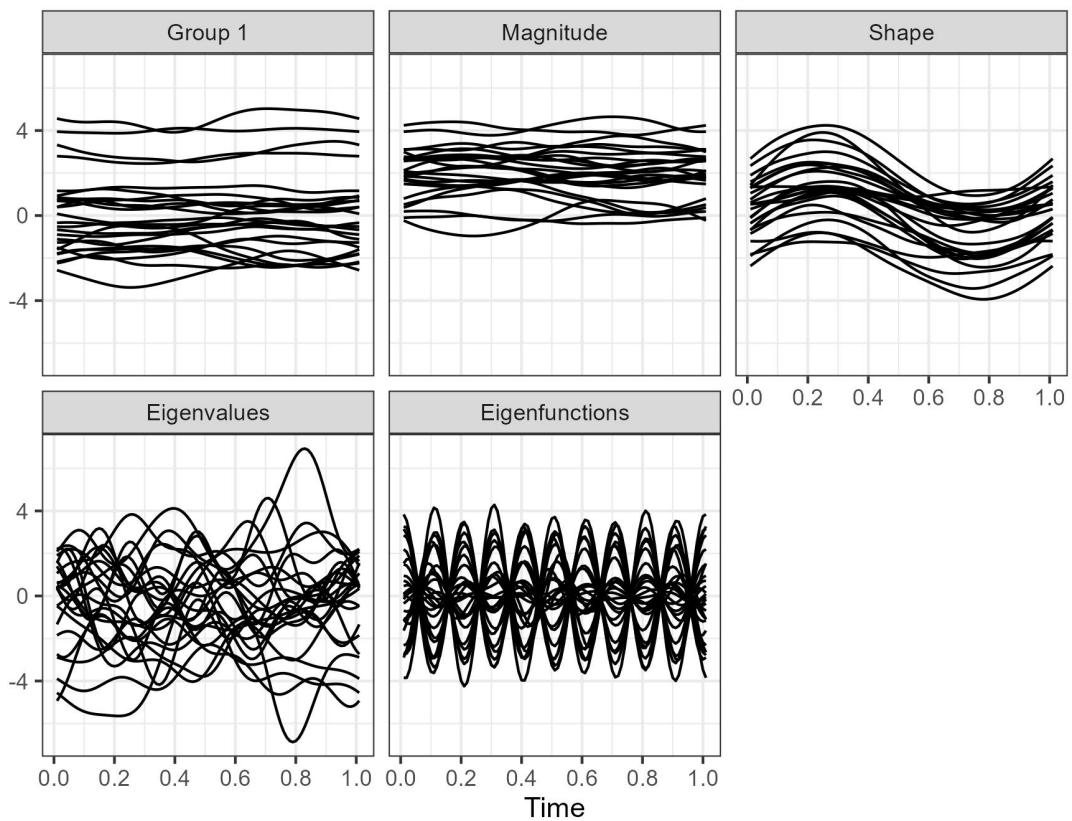


Figure B.9: *Hypothesis testing: Simulated datasets generated under Models (T_1) – (T_4) , as described in Section 4.3. Each panel contains 20 functional observations. The top left panel represents the reference group, while the remaining panels display the second group of functions differing in magnitude, shape, eigenvalues, and eigenfunctions, respectively.*

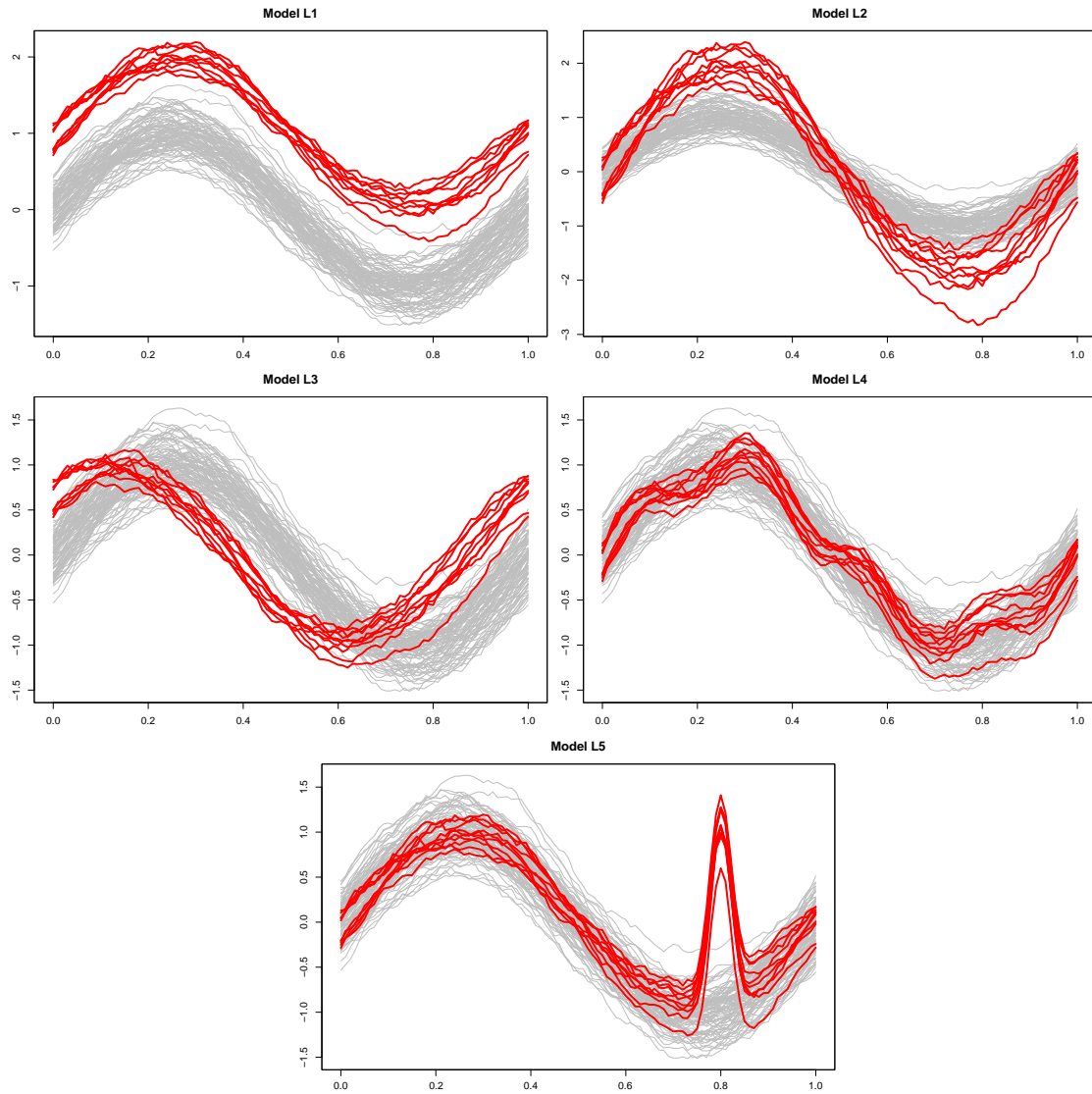


Figure B.10: *Robust location estimation: Simulated datasets generated under the contamination Models (L_1)–(L_5) described in Section 4.4. Each panel contains 100 functions, of which 10 are contaminated. The non-contaminated functions are shown in gray, while the contaminating functions are highlighted in red.*

Model	ε	RPD _{0.1}	RPD _{0.5}	RHD _{0.1}	RHD _{0.5}	FD	MBD	ID	SD
(L ₁)	0.000	7.053 (0.457)	5.063 (0.405)	5.170 (0.565)	5.219 (0.963)	4.379 (0.794)	4.305 (0.639)	4.965 (0.400)	4.493 (0.517)
	0.025	7.226 (0.508)	5.226 (0.492)	5.346 (0.542)	5.405 (0.861)	4.423 (0.854)	4.347 (0.614)	4.994 (0.529)	4.524 (0.539)
	0.050	8.396 (0.492)	5.507 (0.497)	5.927 (0.647)	5.852 (1.047)	4.867 (0.875)	4.748 (0.657)	5.727 (0.432)	4.970 (0.599)
	0.075	8.033 (0.430)	5.796 (0.487)	6.101 (0.503)	6.135 (1.085)	5.206 (0.760)	5.054 (0.520)	5.683 (0.440)	5.179 (0.429)
	0.100	9.391 (0.596)	6.442 (0.382)	6.780 (0.642)	6.651 (1.041)	5.510 (0.711)	5.483 (0.517)	6.528 (0.417)	5.553 (0.494)
(L ₂)	0.000	7.053 (0.457)	5.063 (0.405)	5.170 (0.565)	5.219 (0.963)	4.379 (0.794)	4.305 (0.639)	4.965 (0.400)	4.493 (0.517)
	0.025	7.200 (0.457)	5.278 (0.472)	5.515 (0.570)	5.359 (1.082)	4.416 (0.858)	4.344 (0.671)	5.111 (0.335)	4.608 (0.606)
	0.050	7.371 (0.368)	5.160 (0.556)	5.637 (0.654)	5.528 (1.457)	4.592 (0.923)	4.482 (0.638)	5.118 (0.432)	4.761 (0.628)
	0.075	7.188 (0.472)	5.271 (0.481)	5.625 (0.630)	5.743 (1.221)	4.876 (0.762)	4.774 (0.477)	5.386 (0.449)	4.878 (0.474)
	0.100	7.194 (0.341)	5.356 (0.338)	5.490 (0.501)	5.940 (1.405)	5.034 (0.715)	5.122 (0.517)	5.831 (0.588)	5.226 (0.525)
(L ₃)	0.000	7.528 (0.402)	5.178 (0.514)	5.331 (0.632)	5.379 (0.992)	4.422 (0.939)	4.343 (0.678)	5.086 (0.397)	4.640 (0.543)
	0.025	7.455 (0.511)	5.118 (0.490)	5.680 (0.492)	5.617 (0.854)	4.557 (0.708)	4.418 (0.524)	4.922 (0.499)	4.553 (0.525)
	0.050	7.650 (0.356)	5.277 (0.458)	5.557 (0.607)	5.525 (0.841)	4.612 (0.946)	4.555 (0.788)	5.245 (0.567)	4.790 (0.581)
	0.075	6.602 (0.575)	5.176 (0.669)	5.623 (0.689)	5.737 (0.849)	4.915 (1.215)	4.811 (0.993)	5.565 (0.658)	4.960 (0.746)
	0.100	7.237 (0.553)	5.426 (0.536)	5.754 (0.596)	5.854 (0.976)	5.217 (1.084)	5.143 (0.912)	5.954 (0.907)	5.368 (0.777)
(L ₄)	0.000	6.884 (0.512)	5.139 (0.443)	5.604 (0.584)	5.372 (0.927)	4.442 (0.938)	4.312 (0.634)	4.890 (0.406)	4.444 (0.479)
	0.025	7.088 (0.463)	5.130 (0.449)	5.333 (0.623)	5.623 (1.034)	4.505 (0.857)	4.354 (0.683)	5.026 (0.443)	4.705 (0.527)
	0.050	7.665 (0.371)	5.054 (0.450)	5.301 (0.532)	5.643 (0.928)	4.449 (0.758)	4.349 (0.620)	5.103 (0.428)	4.589 (0.473)
	0.075	7.774 (0.310)	5.651 (0.458)	5.539 (0.683)	5.635 (0.850)	4.675 (0.714)	4.588 (0.474)	5.175 (0.369)	4.737 (0.462)
	0.100	7.244 (0.424)	5.173 (0.428)	5.489 (0.580)	5.644 (0.902)	4.552 (0.865)	4.473 (0.667)	5.123 (0.364)	4.741 (0.528)
(L ₅)	0.000	7.139 (0.525)	4.920 (0.603)	5.328 (0.600)	5.324 (1.068)	4.430 (0.988)	4.293 (0.750)	4.870 (0.511)	4.495 (0.663)
	0.025	6.996 (0.413)	5.001 (0.439)	5.617 (0.663)	5.381 (0.970)	4.292 (0.610)	4.221 (0.470)	4.779 (0.351)	4.463 (0.505)
	0.050	7.415 (0.369)	5.343 (0.394)	6.328 (0.653)	5.688 (1.208)	4.493 (1.008)	4.396 (0.589)	4.848 (0.390)	4.811 (0.467)
	0.075	7.560 (0.405)	5.256 (0.386)	6.363 (0.685)	5.881 (1.349)	4.786 (1.523)	4.400 (0.694)	5.087 (0.352)	4.975 (0.678)
	0.100	7.040 (0.467)	5.285 (0.487)	6.467 (0.641)	5.998 (1.202)	4.813 (1.441)	4.476 (0.709)	5.088 (0.360)	4.946 (0.794)

Table B.6: *Robust location estimation: A comprehensive comparison of performance measures. The table reports $\text{MISE} \cdot 10^3$ defined in (16) for contamination models described in Section 4.4. For each experimental setting, the deepest function is computed and the corresponding quantities are evaluated. The table reports Monte Carlo averages with standard deviations in parentheses, based on 500 simulations.*

Model	ε	RPD _{0.1}	RPD _{0.5}	RHD _{0.1}	RHD _{0.5}	FD	MBD	ID	SD
(L ₁)	0.000	0.006 (0.008)	0.009 (0.010)	0.006 (0.010)	0.007 (0.012)	0.013 (0.014)	0.008 (0.011)	0.017 (0.020)	0.006 (0.012)
	0.025	0.039 (0.023)	0.110 (0.049)	0.092 (0.046)	0.041 (0.036)	0.063 (0.032)	0.066 (0.033)	0.093 (0.035)	0.049 (0.031)
	0.050	0.366 (0.093)	0.279 (0.078)	0.411 (0.100)	0.200 (0.081)	0.270 (0.086)	0.286 (0.074)	0.477 (0.112)	0.306 (0.073)
	0.075	0.796 (0.204)	0.479 (0.129)	0.706 (0.170)	0.352 (0.109)	0.539 (0.158)	0.539 (0.129)	0.724 (0.178)	0.438 (0.123)
	0.100	0.981 (0.121)	0.918 (0.207)	1.287 (0.197)	0.690 (0.144)	0.985 (0.136)	0.995 (0.123)	1.355 (0.151)	0.928 (0.224)
(L ₂)	0.000	0.006 (0.008)	0.009 (0.010)	0.006 (0.010)	0.007 (0.012)	0.013 (0.014)	0.008 (0.011)	0.017 (0.020)	0.006 (0.012)
	0.025	0.009 (0.009)	0.011 (0.013)	0.019 (0.026)	0.018 (0.017)	0.028 (0.027)	0.026 (0.025)	0.028 (0.030)	0.021 (0.023)
	0.050	0.065 (0.054)	0.061 (0.044)	0.072 (0.080)	0.045 (0.044)	0.108 (0.060)	0.110 (0.065)	0.105 (0.070)	0.132 (0.093)
	0.075	0.113 (0.093)	0.128 (0.100)	0.169 (0.100)	0.120 (0.105)	0.308 (0.171)	0.309 (0.182)	0.306 (0.191)	0.264 (0.166)
	0.100	0.140 (0.111)	0.265 (0.180)	0.284 (0.169)	0.235 (0.138)	0.511 (0.302)	0.582 (0.338)	0.643 (0.374)	0.508 (0.338)
(L ₃)	0.000	0.018 (0.017)	0.025 (0.024)	0.019 (0.019)	0.010 (0.010)	0.015 (0.013)	0.015 (0.014)	0.013 (0.014)	0.009 (0.013)
	0.025	0.052 (0.047)	0.034 (0.035)	0.007 (0.012)	0.009 (0.012)	0.026 (0.026)	0.029 (0.029)	0.037 (0.037)	0.034 (0.042)
	0.050	0.033 (0.035)	0.053 (0.051)	0.045 (0.039)	0.037 (0.041)	0.143 (0.109)	0.145 (0.095)	0.194 (0.145)	0.201 (0.160)
	0.075	0.084 (0.088)	0.109 (0.094)	0.052 (0.045)	0.062 (0.073)	0.284 (0.179)	0.265 (0.172)	0.370 (0.222)	0.357 (0.288)
	0.100	0.130 (0.109)	0.162 (0.130)	0.135 (0.114)	0.104 (0.103)	0.568 (0.360)	0.574 (0.361)	0.640 (0.434)	0.645 (0.509)
(L ₄)	0.000	0.015 (0.015)	0.021 (0.017)	0.011 (0.016)	0.026 (0.030)	0.006 (0.008)	0.007 (0.011)	0.017 (0.021)	0.005 (0.007)
	0.025	0.005 (0.007)	0.010 (0.009)	0.011 (0.013)	0.014 (0.016)	0.006 (0.014)	0.007 (0.011)	0.008 (0.010)	0.007 (0.008)
	0.050	0.049 (0.049)	0.022 (0.021)	0.019 (0.029)	0.014 (0.018)	0.007 (0.011)	0.007 (0.008)	0.013 (0.017)	0.010 (0.012)
	0.075	0.020 (0.026)	0.015 (0.018)	0.013 (0.024)	0.009 (0.008)	0.010 (0.012)	0.013 (0.014)	0.011 (0.019)	0.010 (0.011)
	0.100	0.018 (0.026)	0.020 (0.022)	0.023 (0.025)	0.025 (0.030)	0.022 (0.029)	0.020 (0.021)	0.010 (0.012)	0.020 (0.024)
(L ₅)	0.000	0.006 (0.009)	0.009 (0.013)	0.009 (0.011)	0.015 (0.013)	0.008 (0.013)	0.006 (0.009)	0.011 (0.011)	0.005 (0.006)
	0.025	0.004 (0.005)	0.044 (0.030)	0.033 (0.039)	0.052 (0.066)	0.033 (0.020)	0.038 (0.029)	0.027 (0.021)	0.047 (0.046)
	0.050	0.016 (0.020)	0.016 (0.031)	0.021 (0.033)	0.038 (0.050)	0.009 (0.011)	0.006 (0.007)	0.008 (0.013)	0.083 (0.160)
	0.075	0.033 (0.061)	0.075 (0.130)	0.080 (0.132)	0.086 (0.104)	0.029 (0.058)	0.026 (0.046)	0.026 (0.034)	0.190 (0.387)
	0.100	0.038 (0.097)	0.038 (0.074)	0.049 (0.098)	0.149 (0.143)	0.022 (0.048)	0.020 (0.032)	0.029 (0.042)	0.233 (0.484)

Model	ε	RPD _{0.1}	RPD _{0.5}	RHD _{0.1}	RHD _{0.5}	FD	MBD	ID	SD
(L ₁)	0.000	6.990 (0.453)	5.014 (0.403)	5.122 (0.558)	5.171 (0.955)	4.331 (0.790)	4.262 (0.635)	4.908 (0.401)	4.451 (0.516)
	0.025	7.129 (0.509)	5.075 (0.478)	5.212 (0.549)	5.322 (0.859)	4.325 (0.839)	4.246 (0.613)	4.861 (0.536)	4.439 (0.538)
	0.050	7.966 (0.468)	5.186 (0.495)	5.471 (0.654)	5.607 (1.056)	4.561 (0.888)	4.426 (0.669)	5.207 (0.452)	4.626 (0.609)
	0.075	7.179 (0.364)	5.275 (0.479)	5.352 (0.490)	5.737 (1.111)	4.630 (0.713)	4.478 (0.496)	4.920 (0.409)	4.703 (0.405)
	0.100	8.343 (0.609)	5.480 (0.366)	5.449 (0.613)	5.914 (1.070)	4.489 (0.702)	4.452 (0.528)	5.132 (0.349)	4.588 (0.493)
(L ₂)	0.000	6.990 (0.453)	5.014 (0.403)	5.122 (0.558)	5.171 (0.955)	4.331 (0.790)	4.262 (0.635)	4.908 (0.401)	4.451 (0.516)
	0.025	7.133 (0.458)	5.225 (0.470)	5.452 (0.560)	5.299 (1.078)	4.353 (0.850)	4.284 (0.663)	5.043 (0.332)	4.551 (0.594)
	0.050	7.247 (0.394)	5.059 (0.550)	5.521 (0.642)	5.440 (1.425)	4.448 (0.925)	4.336 (0.636)	4.973 (0.439)	4.592 (0.630)
	0.075	7.018 (0.432)	5.102 (0.461)	5.412 (0.607)	5.578 (1.206)	4.532 (0.733)	4.429 (0.501)	5.040 (0.376)	4.577 (0.472)
	0.100	6.997 (0.333)	5.050 (0.414)	5.164 (0.499)	5.659 (1.354)	4.487 (0.726)	4.504 (0.461)	5.146 (0.339)	4.679 (0.477)
(L ₃)	0.000	7.450 (0.400)	5.112 (0.513)	5.269 (0.626)	5.326 (0.979)	4.372 (0.931)	4.294 (0.674)	5.032 (0.396)	4.594 (0.540)
	0.025	7.343 (0.524)	5.043 (0.487)	5.627 (0.487)	5.563 (0.849)	4.494 (0.705)	4.355 (0.517)	4.845 (0.480)	4.482 (0.514)
	0.050	7.556 (0.354)	5.182 (0.450)	5.468 (0.612)	5.444 (0.831)	4.434 (0.936)	4.374 (0.754)	5.011 (0.544)	4.552 (0.515)
	0.075	6.466 (0.515)	5.027 (0.628)	5.526 (0.669)	5.629 (0.816)	4.595 (1.120)	4.510 (0.884)	5.153 (0.489)	4.567 (0.586)
	0.100	7.050 (0.484)	5.222 (0.461)	5.574 (0.587)	5.703 (0.958)	4.612 (0.875)	4.533 (0.666)	5.271 (0.544)	4.684 (0.511)
(L ₄)	0.000	6.814 (0.503)	5.077 (0.445)	5.548 (0.581)	5.303 (0.916)	4.400 (0.931)	4.270 (0.629)	4.834 (0.392)	4.403 (0.474)
	0.025	7.026 (0.458)	5.079 (0.446)	5.279 (0.617)	5.564 (1.025)	4.463 (0.852)	4.313 (0.678)	4.978 (0.438)	4.660 (0.522)
	0.050	7.555 (0.361)	4.992 (0.445)	5.239 (0.512)	5.583 (0.911)	4.406 (0.750)	4.307 (0.612)	5.049 (0.417)	4.542 (0.466)
	0.075	7.692 (0.298)	5.590 (0.455)	5.481 (0.666)	5.581 (0.845)	4.627 (0.707)	4.538 (0.470)	5.123 (0.364)	4.689 (0.456)
	0.100	7.169 (0.409)	5.112 (0.418)	5.422 (0.575)	5.574 (0.886)	4.493 (0.842)	4.417 (0.653)	5.071 (0.359)	4.684 (0.515)
(L ₅)	0.000	7.076 (0.521)	4.872 (0.594)	5.276 (0.591)	5.266 (1.060)	4.386 (0.979)	4.253 (0.743)	4.820 (0.507)	4.454 (0.656)
	0.025	6.936 (0.409)	4.917 (0.433)	5.539 (0.657)	5.286 (0.980)	4.225 (0.608)	4.149 (0.469)	4.714 (0.351)	4.381 (0.494)
	0.050	7.340 (0.358)	5.284 (0.395)	6.256 (0.661)	5.604 (1.232)	4.448 (1.002)	4.354 (0.586)	4.801 (0.384)	4.690 (0.438)
	0.075	7.467 (0.414)	5.139 (0.351)	6.233 (0.726)	5.749 (1.375)	4.718 (1.471)	4.339 (0.691)	5.020 (0.333)	4.747 (0.500)
	0.100	6.945 (0.426)	5.204 (0.471)	6.366 (0.692)	5.802 (1.252)	4.753 (1.395)	4.420 (0.703)	5.018 (0.350)	4.675 (0.589)

Table B.7: *Robust location estimation: A comprehensive comparison of performance measures. The upper panel reports $ISB \cdot 10^3$, while the lower panel reports $IVAR \cdot 10^3$, both defined in (16) for contamination models described in Section 4.4. For each experimental setting, the deepest function is computed and the corresponding quantities are evaluated. The table reports Monte Carlo averages with standard deviations in parentheses, based on 500 simulations.*